A tour of high energy physics: from quantum field theory to Higgs coupling measurements at the LHC

by

Evan Ranken

Submitted in Partial Fulfillment of the

Requirements for the Degree

Doctor of Philosophy

Supervised by Professor Regina Demina

Department of Physics and Astronomy

Arts, Sciences and Engineering

School of Arts and Sciences

University of Rochester

Rochester, New York

2020

Table of Contents

Biographical Sketch

Evan Ranken grew up in the small town of Bernalillo, New Mexico (USA). It is not far from Albuquerque, a city best known as the setting of the prestige television drama *Breaking Bad*.

The following publications were a result of work conducted during doctoral study:

- Measurement of the top quark Yukawa coupling using kinematics of $t\bar{t}$ dilepton decays at $\sqrt{s}$= 13 TeV

  with Regina Demina and the CMS collaboration (In preparation)

- Highly nonlinear wave solutions in a dual to the chiral model

  with S.G. Rajeev Phys. Rev. D 93 105016 [arXiv:1603.08256]

- Continuity of scalar fields with logarithmic correlations

  With S.G. Rajeev. Phys. Rev. D 92 045021 [arXiv:1508.04655]

Acknowledgements

The author would like to thank all the teachers who inspired and helped during his youth in New Mexico, including: Stuart Lipkowitz, Dr. Vraspir, Danny Packer, Dr. Buchanan, Dr. Julian, Mr. Montaño... and so many more!

Thanks to everyone in the Physics & Mathematics (& Computer Science) departments at Colorado College circa 2012, with extra special thanks to Stefan Erickson, Shane Burns, Stephanie Dicenzo, Marlow Anderson, David Brown, Phillip Cervantes, Dick Hilt, and Marita Beckert.

At Rochester, thanks to my research collaborators and to Laura Blumkin, without whom the department would fall apart. Thanks as well to the best housemates ever, Joe Murphree and Amanda Davis, and to everyone else who helped with the self-paced curriculum.

Thanks to Brajesh Gupt and Param Singh for introducing me to the world of research in physics over the summer of 2011.

Special thanks to Kaila Ryan for so many things, as well as John Derksen and Griffin Gorsky for providing lodging during a difficult time in Boston in 2019. Thanks to Aku Antikainen and Meghan Dorn for similar help in late 2018. And thanks to everyone else who supported me during that time.

And of course, thanks to my parents Bill & Bev Ranken, who have supported me through every smart and stupid thing I have done. Love you!

Abstract

This document summarizes work in theoretical and experimental high-energy physics completed as part of the author's doctoral studies. Beginning with an overview of the relevant backgrounds, the motivation for this doctoral research is explored through discussion of the current state of particle physics and many of the unanswered questions driving research in this field. Emphasis is placed on providing context for doctoral research to readers outside of the particle physics community. Theoretical work from early PhD studies is summarized, exploring the continuity of scalar quantum fields and studying a novel toy field theory with intriguing nonlinear wave solutions. Recent research in experimental particle physics is presented in further detail, and a measurement is presented in collaboration with the CMS experiment located at CERN. This measurement quantifies the strength of interaction between the top quark and Higgs boson, obtaining a Yukawa coupling value of $Y_{\mathrm{t}} = 1.16^{+0.24}_{-0.36}$ relative to the standard model.

Contributors and Funding Sources

This work was supervised by a dissertation committee consisting of Professors Regina Demina (advisor), S.G. Rajeev, and Arie Bodek of the Physics & Astronomy Department, as well as Professor Alan Grossfield of the Department of Biochemistry and Biophysics.

All theoretical research from 2014-2016 was done in close collaboration with S.G. Rajeev. Experimental research was performed from 2017-2020 with the CMS collaboration, using a reconstruction framework developed by Otto Hindrichs, who also provided useful guidance and tools to assess uncertainties and model detector effects within that framework. All other work for the dissertation was completed by the author independently.

This work was made possible by a wide variety of independent software projects, including: Mathematica, (CERN) ROOT, RooFit, and RootStat; as well as free and open source software like the GNU/Linux system and the Python programming language.

Specific physics simulation tools are cited individually.

Experimental work also relied on computing resources located at Fermi National Accelerator Laboratory (Fermilab), and the European Center for Nuclear Research (CERN).

Graduate study was supported by the U.S. Department of Energy Office of Science, under Award Number DE-SC0008475 as well as the NSF Graduate Research Fellowship Program under Grant No. DGE-141911, and by teaching assistantships and the Sproull fellowship at the University of Rochester.

List of Tables

List of Figures

Introduction

What is this dissertation about, and why should you care?

Those are both good questions. The goal of this document is to take the author's graduate research, which often addresses hyper-specific questions encased in jargon, and present it in the broader context of current physics knowledge. The research in question involves both experimental and theoretical projects in an area frequently labeled *high energy physics*, a subset of particle physics. In a sense, this branch of physics aims to answer fundamental questions involving the smallest known pieces of the universe. The essential nature of these fundamental particles becomes increasing evident at smaller distances and higher energies–which is why the theoretical scope of high energy physics is quite broadly defined. On the experimental side, the label is more commonly reserved for experiments at large particle colliders.

At its heart, all the research involved in this dissertation shares the common goal of better understanding these fundamental particles and the rules that govern them. To contextualize these studies, we will try to summarize the current state of the field and explain the lingering questions that these research projects seek to answer. We are guided by a rather bombastic question: What is the universe made of at the most fundamental level? The author hopes that anyone with an interest in this question will find something of value in this document, even if the research involved reveals only a hint of a tiny piece of an answer.

0.1 An overview of what's to follow

We begin in Chapter 1 with an overview of modern particle physics, followed by a discussion of open problems in the field in Chapter 2. The content of these chapters will already be familiar to anyone with experience in particle physics, so they are written with a non-expert in mind as much as possible, while still covering the necessary material. We then proceed to discuss theoretical avenues of research in Chapter **??**, including an overview of theoretical research completed by the author in the early years of doctoral study, rooted in the detailed mathematical study of quantum fields. Next we set our sights on experiment, giving a brief overview of experimental avenues in modern particle physics in Chapter 4 before giving a primer on the role of top quarks in particle experiments in Chapter 5. We then discuss the LHC apparatus and CMS experiment in Chapter 6, before concluding with a summary of the author's final doctoral research project, a measurement of the top quark Yukawa coupling, in Chapter 7.

Effort has been made to keep the majority of this thesis as accessible as possible to a wide scientific audience, to the best of the author's ability. A majority of technical details are confined to Chapters **??** and 7, though other sections may delve briefly into more precise language to offer clarity to the expert reader while offering references to the non-expert.

Chapter 1

A primer on particle physics

1.1 The big picture

It is often said that fundamental physics has two pieces which are at conflict with one another: quantum physics and general relativity. The former describes the smallest building blocks of the universe, while the latter explains its behavior at the largest scales. This thesis is concerned with the former, but it is useful to have a broad idea of how the two contrast with one another.

General relativity provides a unified framework for explaining gravitational interaction at large scales. It superseded Newton's theory of gravity, which already did a fine job at explaining most planetary and lunar orbits, along with earthly phenomena such as projectile motion and blocks sliding down frictionless ramps. Meanwhile, general relativity gave us the big bang theory, explaining much about the universe's origins and its behavior on large scales. It even predicted the possibility of extreme objects such as black holes, which have now been observed through a variety of means.

But general relativity is a theory which operates at almost incomprehensibly different scales than that of particle physics. And rather than provide a mechanism to explain gravity on small scales, particle physics ignores it completely. Our current understanding of particle physics fails to provide a small-scale origin for gravitational force, and breaks down upon attempt to forcefully include gravity. This discrepancy persists in part because it remains essentially impossible to probe the small scale nature of gravitational interaction in a lab setting. Other forces typically render gravity obsolete at small scales. Only a few extreme cases directly require a simultaneous description of quantum physics and gravity, such as the centers of black holes or the very moment of the big bang. These are of course inaccessible to direct measurement, and the energies involved are almost unfathomable.

Since these extreme scenarios are so incredibly far away from our lab capabilities, one might ask why particle physicists bother to build large machines which operate at a fraction of the energy scale. Luckily, this fundamental contradiction is not the only mystery remaining in particle physics. While General relativity provides a streamlined and unified framework for all large scale interactions in our universe, our model of particle physics is much messier and ad-hoc. It almost begs to be studied further, presenting such apparent disorganization that one suspects immediately something is amiss. And so, within particle physics, there are a number of avenues that could point to breakthroughs in our understanding of fundamental physics. To understand these avenues of research, we present a summary of our current best understanding of particle physics, starting with its predecessors.

1.2 When things got weird: quantum mechanics

In the early 20th century, the development of quantum mechanics radically shook humanity's understanding of the behavior and composition of matter at small scales. Evidence-based models for atoms had gained prevalence in the century prior, but patterns in their structure and behavior remained mysterious. The turn of the century brought the discovery of electrons and protons, which provided more fundamental and universal pieces of matter, although the way they bound to form atoms was far from obvious. The idea of matter consisting of very small discrete pieces was not new, but the strange behavior of the pieces came as a surprise.

Before quantum mechanics, tiny pieces of matter were thought of as *particles* which behaved like tiny billiard balls, while seemingly separate phenomena like light (electromagnetic radiation) were modeled strictly as *waves*. Einstein's study of the photo-electric effect [2] showed that in fact light behaves at times like a particle, and transmitting energy not continuously but rather by discreet lumps or *quanta*. This was the first hint that light itself is made up of many small particles, now called photons. On the other hand, the famous double slit experiment (though not demonstrated until the 1961) showed that matter particles like electrons could in fact behave like waves to produce interference pattern. [3, 4] In fact, at the smallest scales, matter and light were comprised neither of particles nor waves in the usual sense. Instead, small-scale physics could only accurately be modeled by strange objects with a mixture of particle-like and wave-like properties. This was the dawn of quantum physics. The study of this duality and its implications has proceeded alongside the development of more advanced models of particle physics, and continues to this day. In terms of casual description, the term *particle* stuck, probably because it conveys their quantized nature more intuitively. And so today, we build particle colliders–though a pedantic individual could have dubbed them wave colliders instead.

In quantum mechanics, particles like electrons, protons, or photons are the fundamental objects. By including the known "shape" of the electrostatic force F, which decays over a distance r as $F \propto \frac{1}{r^2}$, this theory was able to model what happens when you take trap a collection of electrons in "orbit" around a positively charged nucleus made of protons and neutrons. Such a collection of fundamental objects stuck together by interaction is called a *bound state*. In doing so, the theory successfully predicted the structure of the periodic table, and many properties of the elements therein. As a novel consequence of the theory, electrons orbiting a nucleus were restricted to certain discrete values of orbital energy and angular momentum. This could be used to explain the energies of emitted photons from many elements, though it did not explain the physical law that allowed a photon to be emitted in the first place. And this was a hint of what the theory lacked–it knew that particles could sometimes be created seemingly out of nothing, as long as energy was conserved. But why this was allowed remained somewhat mysterious.

In a sense, breaking down quantities like energy into small, finite quanta is at the heart of quantum mechanics. Of course, the full story is quite a bit more complicated, and the "true meaning" of consequences is still fiercely debated. Quantum physics is inherently probabilistic, a fact which will carry over to modern particle physics. Second, and instrumental this probabilistic doctrine, is the importance of operators.

In quantum mechanics, observable quantities are described by mathematical operators. Consider a particle in a quantum state, denoted $|\psi\rangle$. We don't think of of observables like position x or momentum p as being simple properties belonging to this particle; rather, they are promoted to operators denoted $\hat{x}$ and $\hat{p}$ which *act* on the particle's quantum state. Probabilistic calculations can be be performed, such as the expectation value of an observable like x or x^2 for a particle with state $|\psi\rangle$. These would be written as $\langle\psi|\,\hat{x}\,|\psi\rangle$, and $\langle\psi|\,\hat{x}^2\,|\psi\rangle$, respectively. Because the particle represented by $|\psi\rangle$ has a distribution of possible measured x-positions, note that $\langle\psi|\,\hat{x}\,|\psi\rangle^2 \neq \langle\psi|\,\hat{x}^2\,|\psi\rangle$. Rather, the two related to calculating the mean and variance of a statistical distribution. We mention these calculations to compare with field theory later on.

1.3 The leap to fields

Quantum field theory (QFT) is often described as the marriage of quantum mechanics with Einstein's theory of special relativity. Although many of the new ideas presented by QFT are a consequence of joining these two theories, it is easy to understand them without discussing special relativity much at all.

A particle is typically thought of as an object that exists at a specific point in space at a given time, while a field is something that has a value at each point in space simultaneously at a given time. The *values* at each point can be scalars, vectors, or more exotic objects. Classical field theory was often used to discuss gravitational and electromagnetic fields, which carry forces felt by classical objects and even by particles in the context of quantum mechanics. The simplest type of field to imagine is a *scalar field* $\phi : \mathbb{R}^d \mapsto \mathbb{R}$. The object ϕ assigns a real number to each point in d-dimensional space. Simple attempts to place a quantum scalar field into relativistic spacetime yield the Klein Gordon equation,

$$\frac{\partial^2}{\partial t^2}\phi - \nabla^2\phi + m^2\phi = 0. \tag{1.1}$$

In relativistic notation, derivatives with respect to the 4 spacetime coordinates t, x, y, z are indexed by μ and repeated instances of μ indicate summation with respect to the Minkowski metric. Using the shorthand ∂_μ for the derivative $\frac{\partial}{\partial x^\mu}$, the Klein Gordon equation can be written as

$$\partial^\mu\partial_\mu\phi + m^2\phi = 0. \tag{1.2}$$

This follows directly from an object called a *Lagrangian density* $\mathscr{L}$, where

$$\mathscr{L} = \partial^\mu\phi\partial_\mu\phi - m^2\phi^2. \tag{1.3}$$

In field theory, basic properties of fields can be read off from the Lagrangian with minimal effort. This particular Lagrangian has two terms: first the *kinetic term* $\partial^\mu\phi\partial_\mu\phi$, also called the free field term. Such a term is present for all sorts of fields, and represents the field's kinetic energy. Unsurprisingly then, the remainder is called the *potential term*, and encodes the field's potential energy. In particular, a term of form $m^2\phi^2$ is called a *mass term*. The mass term, in brief, tells us that the field has some internal energy stored as a mass m. If we *quantize* this field, the meaning of the mass term becomes more interesting.

In QFT, all fields have a ground state or *vacuum state* with the lowest possible energy. The excited states of a field with a mass term are particles with mass m. This encapsulates one of the biggest revolutions brought by QFT: rather than being taken as immutable objects dropped into force-carrying fields, particles themselves are excited states of quantum fields. The number of particles is promoted to quantum operator, through a process known as *second quantization*. The details of this procedure are beyond the scope of this dissertation, but the consequence is simple and groundbreaking: particles can be created and destroyed within the theory.

1.4 Gauge theories and particle interaction

One of the earliest successful models in QFT came from the Dirac equation, describing a more complicated type of field which assigns an object called a *spinor* to each point in spacetime. Spinors describe quantum objects with the attribute of *spin*, thought of as an intrinsic angular momentum. The Dirac equation describes a field ψ with spin 1/2, a type of *fermionic* field. In standard relativistic notation, the Dirac equation reads

$$(i\gamma^\mu\partial_\mu - m)\psi = 0, \tag{1.4}$$

where γ^μ are the famous dirac matrices which make possible the relativistic invariance of a spin-1/2 field. The equation follows from the Lagrangian density

$$\mathscr{L} = i\bar{\psi}\gamma^\mu\partial_\mu\psi - m\bar{\psi}\psi, \tag{1.5}$$

where $\bar{\psi} = \psi^\dagger\gamma^0$ is called the adjoint spinor. Though it looks a bit different than the Lagrangian in (1.3), it has the same fundamental pieces: a kinetic term and a mass term. The Dirac equation was meant to describe electrons, and had a great success in predicting the existence of anti-particles called positrons. However, it is only a starting point for the gauge theories that give us our modern understanding of how particles interact to generate forces. Examining the Lagrangian, we see it has a global symmetry under the transformation

$$\psi \rightarrow e^{i\alpha}\psi. \tag{1.6}$$

In the language of group theory, this is a $U(1)$ symmetry–the same mathematical structure as a symmetry under rotation, though the rotation does not occur in physical space. If the field is altered globally throughout spacetime by a phase α, nothing changes. But in relativity, the field cannot communicate instantaneously from one point to another. So, one could ask how the field “knows" to have the same phase at all locations. Though this sounds like philosophical nitpicking, there is a proposed solution with profound consequences. We can *promote* the global symmetry to a local symmetry, one which depends on the spacetime coordinates x. The new problem is, in making α a function of spacetime coordinates $\alpha(x)$, we break the global symmetry. Separating out a constant scaling q for later use, and applying the chain rule, we now have the transformation

$$\psi \rightarrow e^{iq\alpha(x)}\psi \tag{1.7}$$

$$\partial_\mu\psi \rightarrow e^{iq\alpha(x)}\partial_\mu\psi + iqe^{iq\alpha(x)}\psi\partial_\mu\alpha(x) \tag{1.8}$$

How can we keep the Lagrangian invariant under such a transformation? We introduce a new field A_μ, called a gauge field, which transforms under a local gauge change according to the rule

$$A_\mu \rightarrow A_\mu + iq\partial_\mu\alpha(x). \tag{1.9}$$

This field can have the effect of cancelling out the unwanted extra term in (1.8), effectively enforcing local gauge invariance. We can now construct the locally gauge invariant Lagrangian,

$$\mathscr{L}_{\text{QED}} = i\bar{\psi}\gamma^{\mu}\partial_{\mu}\psi - m\bar{\psi}\psi - \bar{\psi}\gamma^{\mu}qA_{\mu}\psi - \frac{1}{4}F^{\mu\nu}F_{\mu\nu}\ , \tag{1.10}$$

Where $F_{\mu\nu} = \partial_{\mu}A_{\nu} - \partial_{\nu}A_{\mu}$ is introduced as a gauge-invariant kinetic term for the new field. The old fermion field ψ still has its kinetic and mass terms. The new gauge field A_{μ} is a bosonic field, and has a kinetic term but no mass term. Most interestingly, there is a new term containing both fields: an interaction term, with coupling strength q. Taken as a whole, this Lagrangian describes a massive fermionic field (whose excitations are electrons) interacting with a massless gauge-boson field. The excitations of this gauge field are in fact photons. Our construction of $F^{\mu\nu}$ matches the electromagnetic tensor from classical electrodynamics, and the free gauge term $\frac{1}{4}F^{\mu\nu}F_{\mu\nu}$ is the vacuum term from the Lagrangian formulation of Maxwell's equations.

In essence, the imposition of local gauge invariance yields a Lagrangian for a fully interacting field theory, granting our modern understanding of photons as *gauge bosons* that mediate of the electromagnetic force on the quantum level. This particular gauge theory is called *Quantum Electrodynamics*, or QED for short. The Lagrangian can also be written more compactly in terms of a *gauge-covariant* derivative D_{μ}, which absorbs the gauge field interaction term to create derivative operator which itself transforms appropriately under local gauge change:

$$\mathscr{L}_{\text{QED}} = i\bar{\psi}\gamma^{\mu}D_{\mu}\psi - m\bar{\psi}\psi - \frac{1}{4}F^{\mu\nu}F_{\mu\nu}, \tag{1.11}$$

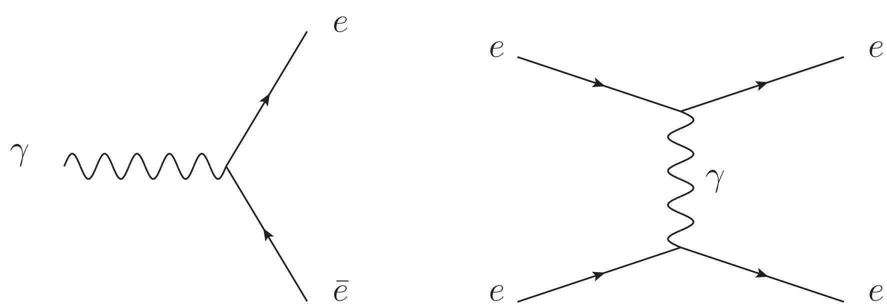

Figure 1.1: Left: Feynman rule for QED diagrams. Feynman diagrams are read with time flowing left to right, with e representing an electron and γ a photon. When the arrow attached to the e line is overall moving leftwards, it is interpreted as a positron $\bar{e}$ as indicated here. Right: a simple process of two electrons interacting via the exchange of a photon.

$$D_\mu = \partial_\mu - iqA_\mu. \tag{1.12}$$

From the QED Lagrangian, we are able not only to read off the basic properties of these fields, but also the specific interaction rules. While we won't explain here how to perform QFT calculations, it was thankfully noted by Richard Feynman that these calculations can be codified as little doodles–now called Feynman diagrams. The doodles are built from individual vertices or *Feynman rules*, and QED has just one, shown in Figure 1.1 (left). The fundamental rule can be thought of as demonstrating the possibility for electrons to emit a photon, or for a photon to produce an electron-positron pair, or for electrons and positrons to annihilate into a photon–all depending how it is rotated. Using these rules, we are able to visualize the physical processes that this model allows, and an example is shown in Figure 1.1 (right).

We pause here to note that the deceptive simplicity of Feynman's doodles hides some ugly truths about the theory. They are in fact *not exactly* accurate depictions

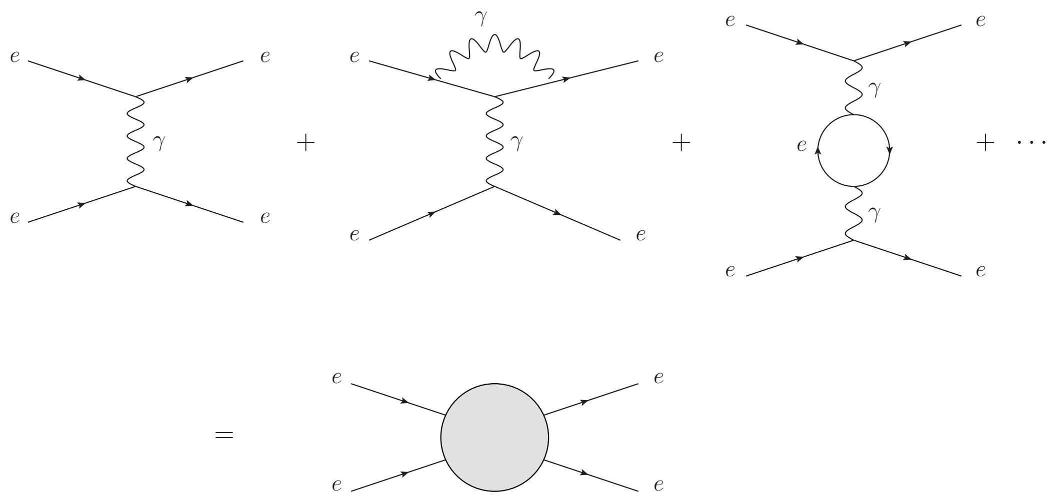

Figure 1.2: Three diagrams are shown in the perturbative expansion for electron-electron scattering. The full process has two electrons ingoing and outgoing–but we do not know exactly what happens in between, as indicated by the grey circle.

of physical processes in the theory–they are terms in a perturbative expansion. Like polynomials in a Taylor series, they each offer us only approximate glimpses of a true quantum field, translating an incomprehensible sea of interactions into individual approximations which can be understood intuitively and calculated. This means also that not all the particles in the feynman diagrams are *real*. The real particles exist in the initial and final states of the diagrams. Anything created and destroyed in between is called a *virtual particle*. Virtual particles are not exactly real and not exactly fake–they are approximations.

For example, Fig. 1.2 shows multiple diagrams for electron-electron scattering in QED. Virtual particles are seen intersecting in closed paths, called loops. The more loops and vertices a feynman diagram has, the harder it is to calculate. Typically, diagrams with two loops are at the cutting edge. But the real process of electron-electron scattering is a combination of all these possibilities.

The accuracy of perturbation theory relies on the electromagnetic coupling strength α. Each vertex in a QED Feynman diagram carries a factor of α for the purposes of most physical calculations (more on this in Chapter **??**). The more interactions present in a diagram, the more factors of α. Furthermore, in QFT, these couplings vary with the energy scale at which they are evaluated–they are called *running couplings*.

Despite the caveats, we are able to approximate many high-energy particle collisions with perturbative calculations in gauge theories where the coupling remains small, and the results agree with nature to a perhaps surprising extent. Luckily, for the electromagnetic interaction, α is generally quite small from the low energies of idle electrons ($\alpha \approx 1/137$) to all the way up to the energies obtained in particle colliders, so the series converges quickly. QED has produced some of the most accurately verified predictions ever made, such as the calculation of the anomalous electron dipole moment, where experiment has verified the accuracy of the theory within 1 part in a trillion [5, 6].

1.5 More gauge theories: the nuclear forces

Gauge theories form the basis of our understanding of particle interaction, giving rise to what are often called fundamental forces in particle physics. The strongest of these interactions is called, rather imaginatively, the *strong interaction* or *strong nuclear force*. It is a gauge theory with symmetry group $SU(3)$, describing the interaction of *quarks* through a force mediated by gauge bosons called *gluons*. Quarks are the tiny pieces which make up protons and neutrons, and the force between them is so strong that it prevents them from flying apart due to electromagnetic repulsion.

$SU(3)$ is a more complicated symmetry group than $U(1)$, with no easy analogy to visualize–some such terminology from group theory will inevitably enter our discussion of gauge theories without proper introduction. For a primer on the essential role that group theory plays in particle physics, the author recommends Ref. [7] or [8].

Rather than a conserved scalar charge q as seen in electrodynamics, quarks carry a three-dimensional analogue called *color charge*. This has led the interaction of quarks and gluons to be called quantum chromodynamics (QCD). $SU(3)$ is a non-Abelian group, meaning the generators do not commute. The Lagrangian at first looks similar to the QED Lagrangian:

$$\mathscr{L}_{\text{QCD}} = i\bar{\psi}^j(\gamma^\mu D_\mu)_j^k \psi_k - m\bar{\psi}^j\psi_j - \frac{1}{4}G_a^{\mu\nu}G_{\mu\nu}^a \, , \tag{1.13}$$

Where ψ is now the fermionic quark field and indices j, k indicate color charge (which is implicitly summed over whenever repeated indices occur, as is our general tradition). The big change comes from the new free gauge field term. This term is related to the commutator of the group elements, so it becomes more complicated in the non-abelian case, and we have had to define

$$G_{\mu\nu}^a = \partial_\mu A_\nu^a - \partial_\nu A_\mu^a + g f_{bc}^a A_\mu^b A_\nu^c \, . \tag{1.14}$$

Here a, b, c index the 8 generators of the $SU(3)$ group that form the corresponding Lie algebra $\mathfrak{su}(3)$, and f^{abc} are called the structure constants of that algebra. g is just a constant. This form of Lagrangian generalizes to non-Abelian gauge theories, known collectively as *Yang-Mills theory*. In fact, the simple case of QED is the exception and not the rule–most physical gauge theories are non-Abelian.

While this might seem very technical, in one sense the fundamental change is simple: $G_a^{\mu\nu}$ indicates that gluons themselves carry color charge, and its third term shows that can self-interact. From a theory standpoint, this makes calculations difficult, and many known properties of QCD are difficult to demonstrate with rigor from the fundamental model.

QCD (along with Yang-Mills theory more generally) has a property called *asymptotic freedom*, which meant that the associated coupling constant α_s becomes small at high energies, and thus and perturbative calculations can describe collisions at particle colliders up to a point (as we will see in Chapter 5). However, the self-interaction of the gauge bosons leads to a situation where the theory is *strongly coupled* over large distances and therefore at low energies. This means that perturbation theory and its glorious Feynman diagrams break down entirely.

This is also why we don't observe quarks or gluons sitting around by themselves in nature–they quickly form into bound states. In fact, we don't observe them alone at particle colliders either–they form bound states before they even reach the detector. When two quarks bind, it is called a meson. When three quarks bind, the resulting particle is called a hadron, a class of particles that includes protons and neutrons. Such bound states can be understood approximately via *effective field theories*, but their properties are incredibly challenging to deduce from the fundamental QCD Lagrangian. Only at high energies, like those achieved at the LHC, do quarks and gluons start to participate in the more fundamental interactions where perturbation theory holds.

The strong force can hold together protons in a nucleus against the repulsive electromagnetic force. Recall that the the standard electromagnetic force falls of with distance r as $F_{\mathrm{EM}} \sim \frac{1}{r^2}$. However, as a consequence of non-perturbative effects and gluon self-interaction, the strength of the strong interaction has an additional exponential dampening term, $F_{\mathrm{QCD}} \sim \frac{1}{r^2} e^{-\kappa r}$, where κ is a constant. Thus, its effects are felt only at the scale of the atomic nucleus. Such a scaling would be expected by a force with a massive mediator boson, and indeed the strong force was originally theorized to be mediated via π-mesons by Hideki Yukawa in 1935 [9]. While this is not true at the most fundamental level, the strong force effectively has a massive mediator boson due to the gluons' inability to travel unperturbed. Lone gluons and quarks will quickly form bound states such as mesons, hadrons, and hypothesized massive collections of interacting gluons called glueballs. However, there is another nuclear force, which is mediated by massive bosons in a more fundamental sense.

The Weak nuclear interaction is the weakest of known particle interactions (not counting gravity which is not yet understood on the particle level), and is responsible for many radioactive decays. Like the strong force, its strength has an exponential damping term confining its effects to the nuclear scale. In this case, the mediator bosons appear to be the massive $\mathrm{W}^{\pm}$ and Z bosons. These mediate interactions, for example, involving electrons and tiny neutral particles called neutrinos. However, for a long time, it was not understood how it is possible for a gauge theory to have massive mediator bosons. The answer here turned out to be more complicated, and would lead to the last missing piece in what is today called the standard model of particle physics.

1.6 The Higgs mechanism and electroweak unification

The Weak force appears to have 3 massive mediator bosons. A gauge theory with an $SU(2)$ symmetry would have the right amount of mediators, but they ought to be massless. It turns out that this can only be explained by unifying the weak force and QED into one interaction, and throwing in a brand new scalar field: the Higgs field.

The Higgs field is a scalar doublet $\phi = \begin{pmatrix} \phi^+ \\ \phi^0 \end{pmatrix}$ where ϕ^+, ϕ^0 are complex. The Higgs Lagrangian should have the standard form

$$L_{\text{Higgs}} = D_\mu \phi^\dagger D^\mu \phi - V(\phi). \tag{1.15}$$

The covariant derivative D_μ must respect the gauge symmetry of electroweak unification, and will turn out to be somewhat messy, so let us focus first on the potential term. In addition to the usual mass term, the Higgs potential contains a fourth order self-interaction term:

$$V(\phi) = \mu^2 \phi^\dagger \phi + \lambda(\phi^\dagger \phi)^2 \tag{1.16}$$

where μ and λ are conventional constants and $\phi^\dagger$ is the Hermitian conjugate of ϕ used to take inner products. In the standard model $\mu^2 < 0$ while $\lambda > 0$. The resulting shape of the Higgs potential is such that the ground state (or vacuum state) occurs when $|\ \phi\ | \neq 0$. The potential can most easily be visualized by visualized by restricting one component, say ϕ^+, to be zero, as shown in in Fig. 1.3. The resulting shape is often referred to as the *Mexican hat* potential by a bunch of European

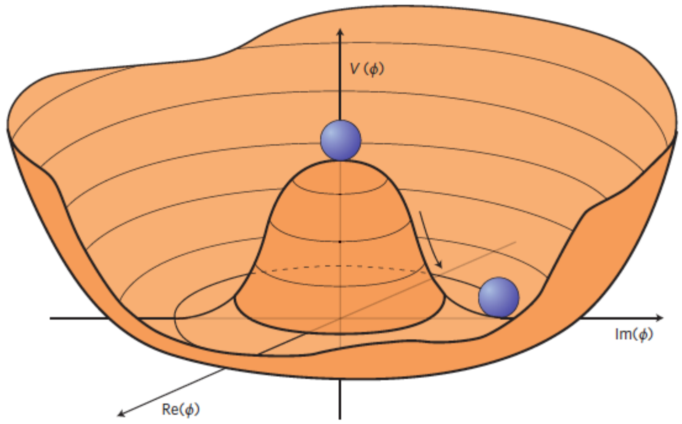

Figure 1.3: A visualization of the Higgs potential, restricted to the one component of the doublet ϕ (courtesy of John Ellis, CERN)

physicists who don't know the word *sombrero*. The Higgs field illustrates a concept called spontaneous symmetry breaking. Though the potential shown in Fig. 1.3 has a rotational symmetry, a ball placed at $\phi = 0$ is in unstable equilibrium, and will roll down in a random direction to break the symmetry. This principle is now essential in our understanding of particle physics, especially in the context of the universe's evolution.

The electroweak sector of the standard model starts out as a standard gauge theory like QED and QCD, with a gauge group that is a product of two symmetries: $SU(2)_I \times U(1)_Y$, which are used to define the gauge covariant derivatives in the Eq. 1.15. The subscripts I and Y stand for the associated conserved quantities *weak isospin* and *weak hypercharge* associated with these symmetries, to distinguish them from other standard model symmetry groups such as $U(1)$ symmetry of QED. This gauge theory should have 4 massless mediators, but it is coupled to the Higgs field. However, as we can see, the ground state of the Higgs field spontaneously breaks this symmetry, giving the field a non-zero value. This breaks the overall gauge symmetry of the model. Gauge bosons mediating interactions between electrons and neutrinos acquire a mass term through the Higgs field's vacuum expectation value. These include the charged W bosons, and the neutral Z boson. The Z boson in fact is a mixture of the original $SU(2)_I$ and $U(1)_Y$ mediators, as is the photon that mediates the remaining $U(1)$ symmetry. Thus, QED is what remains after the breakdown of a greater symmetry, the process of which separates out the weak force with its massive force carriers. The fact that these force carriers are massive dampens the effect of the force over large distances, leaving its effects confined to the scale of the atomic nuclear force–which is why it is considered one of the *nuclear forces*.

It doesn't really matter *which* way the ball rolls down the hill, as the minimum it will find is part of a rotationally symmetric ring. We can see looking at (1.16) that the minimum occurs when $\mid \phi \mid = \frac{|\mu|}{\sqrt{\lambda}} \equiv v$, called the vacuum expectation value. The excited states of this field will thus be perturbations about this vacuum. Because of the symmetry inherent in $V(\phi)$, without loss of generality we can take the ground state to fall such that the first component of ϕ is zero and the second component lies on the real axis. A small excitation of the vacuum state will then look like

$$\phi = \begin{pmatrix} 0 \\ \\ v \end{pmatrix} \rightarrow \begin{pmatrix} 0 \\ \\ v + H \end{pmatrix} \tag{1.17}$$

Upon quantization, this excitation H is the famed Higgs boson, discovered in 2012 at the LHC [10, 11]. The discovery of the particle itself was such a landmark because it verified the much broader model of the Higgs field and the concept of spontaneous symmetry breaking.

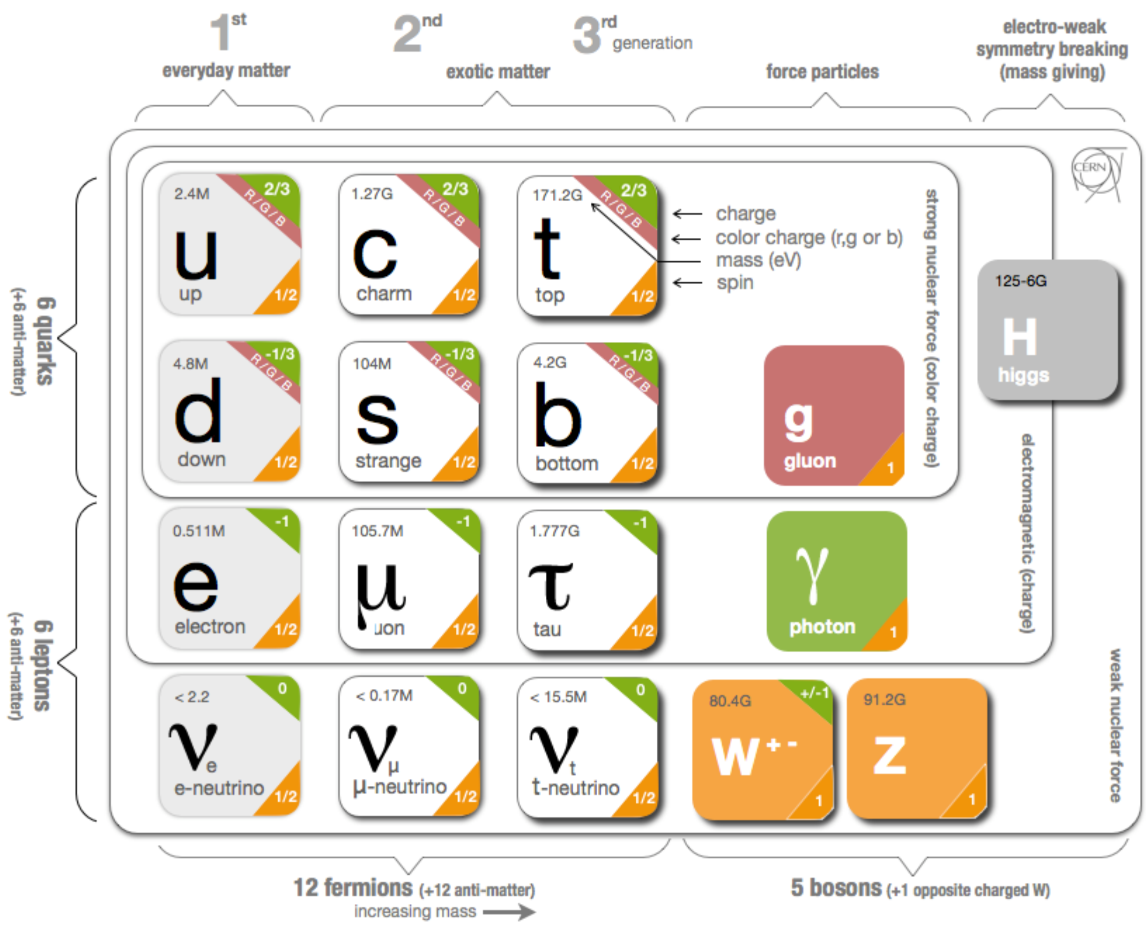

Figure 1.4: A visualization of the standard model of particle physics, courtesy of CERN

1.7 The standard model

The standard model is, essentially, a set of gauge field theories within the framework of QFT. It is the combination in full of the Electroweak interaction (including the Higgs field) and QCD, and is often described as one big gauge theory with symmetry group $SU(3) \times SU(2) \times U(1)$. A summary of the model, and the particles it contains, are shown in Fig. 1.4

A few things are worth noting that have not yet been mentioned. Notably, the standard model contains three generations of matter. Stable electrons have heavier counterparts in the other matter "generations," called muons (μ) and tauons (τ). While these particles are produced in accelerators and in the atmosphere, they are fairly short-lived and decay into lower-mass particles. Similarly, protons and neutrons are made of up and down quarks, which are stable. However, two more generations of heavier quarks exist which can combine into many unstable bound states called exotic hadrons and mesons. The heaviest quark, and the heaviest particle in the standard model, is the top quark, which will be discussed later in this dissertation.

Another thing to mention is *chirality*. Fermions can come with two different types of *chirality*: right-handed, or left handed. Under the the $SU(2)_I$ symmetry in electroweak theory, left-handed fermions transform as a doublet. Specifically, these doublets are formed by combining *up-type* and *down-type* quarks from the same generation:

$$\begin{pmatrix} u \\ d \end{pmatrix}, \begin{pmatrix} c \\ s \end{pmatrix}, \begin{pmatrix} t \\ b \end{pmatrix}; \tag{1.18}$$

or a massive fermion and a neutrino from the same generation,

$$\begin{pmatrix} e \\ \nu_e \end{pmatrix}, \begin{pmatrix} \mu \\ \nu_\mu \end{pmatrix}, \begin{pmatrix} \tau \\ \nu_\tau \end{pmatrix}. \tag{1.19}$$

These same particles are naturally linked by Feynman vertices, such as those shown in 1.5. All quarks and leptons can also come with right-handed chirality, in which

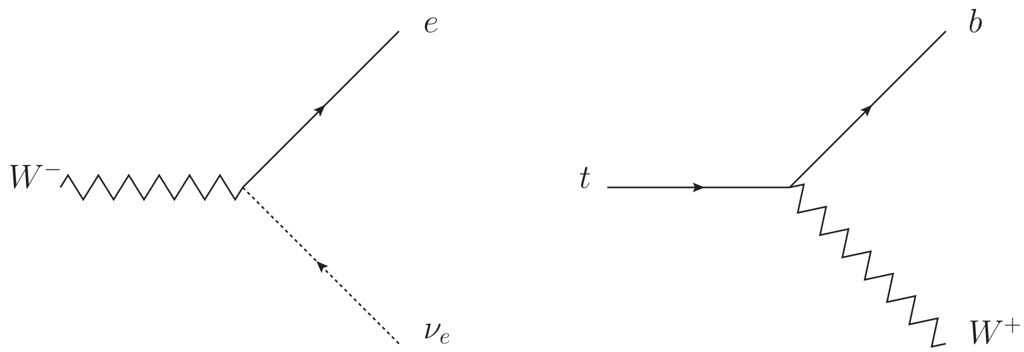

Figure 1.5: Examples of weak interactions involving particles which come together in $SU(2)$ doublets.

case they transform only as a singlet under the action of the $SU(2)_I$, and have a different value of hypercharge Y. While the two chiralities participate in most interactions equally, this is obviously not true for interactions involving a W boson, and there is an even more glaring difference: right-handed neutrinos have not been observed in nature at all, and are not included in the standard model.

1.8 mass in the standard model

On the topic of chirality, there was another profound consequence of the Electroweak unification, which was not originally intended. When writing our the full electroweak Lagrangian, one obviously expects to see mass terms for the massive fermions. In the Dirac Lagrangian (1.5), such a term could be added trivially. However, in the full standard model, a mass term would have to include in equal measure left and right-handed fermions, despite their different transformation properties. A simple number m cannot fulfill this requirement as it does not obey the correct transformation symmetries. The only candidate for a mass term would be a simple linear or *Yukawa*-type coupling between the Higgs field and all massive

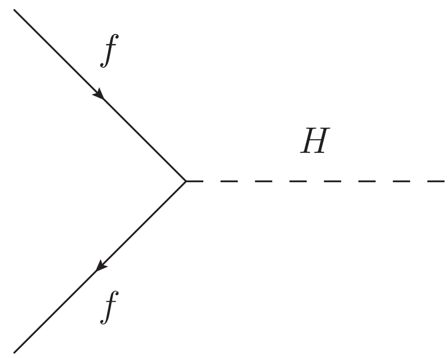

Figure 1.6: A Yukawa interaction vertex between a fermion f and the Higgs boson H

particles. Consider, as an example, the electron. It transforms under an $SU(2)$ doublet L together with ν_e, and a right handed singlet R all by itself. The piece of the standard model Lagrangian containing a Yukawa interaction between an electron and the Higgs field ϕ would read

$$\mathscr{L}_{\text{Yuk}} = -g_e(\bar{L}\phi R + \bar{R}\phi^{\dagger}L) \tag{1.20}$$

After the symmetry breaking in Eq. 1.16, the neutrino field in L drops out and this becomes

$$\mathscr{L}_{\text{Yuk}} = -g_e(\bar{e}_{\text{L}}v\,e_{\text{R}} + \bar{e}_{\text{R}}v\,e_{\text{L}}) - g_e\left(\bar{e}_{\text{L}}\frac{H}{\sqrt{2}}e_{\text{R}} + \bar{e}_{\text{R}}\frac{H}{\sqrt{2}}e_{\text{L}}\right). \tag{1.21}$$

This shows that the resulting mass term comes directly associated with a Yukawa coupling to the Higgs boson H. All massive fermions interact with the Higgs boson in this way,allowing for Feynman vertices such as that shown in Fig. 1.6. Here the interaction strength for a given fermion is the Yukawa coupling constant g_f, and we obtain the mass-Yukawa relation

$$m_f = \frac{g_f\, v}{\sqrt{2}}. \tag{1.22}$$

It is sometimes said that the Higgs boson thus gives mass to all particles, though some would argue that this ignores the subtlety of mass-generation in QCD bound states such as protons, not to mention the mystery of neutrino masses. Either way, the generation of lepton and quark mass through the Higgs mechanism is a core feature of the standard model. It also provides an avenue to test the validity of the standard model, as coupling strengths and mass are typically measured through very different experimental techniques.

In one sense, the idea of fermions acquiring mass from the non-zero vacuum energy density of the Higgs field after spontaneous symmetry breaking is a beautiful and thought-provoking concept. In another sense, it raises more questions than it answers. For example, the fermion masses suggest that the Yukawa coupling values vary by up to 5 orders of magnitude. The top quark, in particular, has $g_\mathrm{t} \approx 1$, while the electron has $g_\mathrm{e} \approx 3 \times 10^{-6}$.

Furthermore, we find that it is impossible for neutrinos to have mass in the standard model through this mechanism. While neutrino mass must be very small based on observation (bounded above by around 10^{-6} times the electron mass), they firmly are known to have non-zero mass based on neutrino flavor-mixing observations. There is no agreed upon way to include such a mass in the standard model, and it remains an open area of study.

1.9 A big, beautiful mess of particles

Unlike general relativity, the standard model is not a single elegant stroke of genius, but rather a mysterious and somewhat haphazard collection of objects. It does not explain why the masses of most particles are what they are, and has at least 26 free parameters with no clear explanation. Nonetheless, whatever it lacks in elegance, it makes up for in reliability. The standard model has outlived many attempts to concoct a more aesthetically pleasing set of objects, and to this date has accurately described the results of decades of particle physics experiments.

There are many ways to summarize the standard model, but it is unavoidably rather complex. It is often said to describe three of the four fundamental forces of nature, with only gravity missing. But this description really steamrolls the complexity of the electroweak interaction, and ignores the subtle role of the Higgs field, which generates arguably an entirely new particle interaction. Furthermore, particle physicists have tried their best to create images (as in Fig. 1.4) which look as minimal as possible, sometimes paving over the fact that the weak interaction has three mediators while gluons come in 8 varieties. Even in this chapter, we have glossed over some subtleties such as CKM mixing and neutrino flavor mixing, which add another layer of complexity to the story.

In many ways, the standard model of particle physics resembles the periodic table, which appeared disorganized and random at the turn of the 20th century, until the theory of quantum mechanics explained its underlying structures. Will we ever see a similar revolution, that provides a more elegant explanation for the structure of the standard model? Perhaps in the 21st century, yet another revalatory idea will change our perspective.

Chapter 2

Unsolved problems in particle physics

"I am a mystery wrapped in an enigma wrapped in a pita. Why the pita? That counts as another mystery."

— Demetri Martin

2.1 Things that are conspicuously missing from the standard model

In many ways, the tension in fundamental physics is driven by apparent incompatibilities between observations at very small scales and observations at very large scales. This goes beyond the fundamental incompatibility of quantum physics and gravity, an issue which becomes evident only when examining singularities appearing in general relativity related to black holes and the big bang. One need only to look at the large scale motion of our own galaxy to see that something is missing in current models.

The rotation curve of the Milky Way, and those of many other spiral galaxies, were found by Vera Rubin and others to differ from their expected behavior in the 1970s, in work that almost certainly should have merited a Nobel Prize (see Ref. [12] for a review). The most obvious explanation is that a large quantity of non-luminous, seemingly invisible matter is floating around throughout our galaxy without interacting much with ordinary matter. Stars and dust that we can see appear to feel its pull through gravity, but do not interact with this mysterious invisible substance, called *dark matter*. If it interacted by the strong or electromagnetic forces, we would be able to detect it. Furthermore, dark matter seems to account for more mass in our universe than ordinary matter.

Since the initial arguments for the existence of dark matter, additional evidence has been found for this substance through gravitational lensing and cosmological models. Many believe that dark matter is made up of heavy particles which interact only weakly, and are missing from the standard model. They could in principle be heavier than what can be directly produced at modern colliders, and interact rarely enough to evade direct detection, being observed only by their gravitational pull. While this is the favored explanation, there could always be something unexpected at play.

On top of this, another mysterious force exists in the universe at even larger scales. While general relativity posits that the universe is expanding ever since the big bang, the rate of expansion seems to be accelerating. This was first observed by the Supernova Cosmology Project [13] and the High-Z Supernova Search [14] in 1998, and implies the presence of yet another mysterious substance pervading the universe, called *dark energy*. This force, unlike all others, seems to push massive bodies apart at large scales.

Curiously, a potential explanation for dark energy is already present with QFT, in the controversial concept of vacuum energy. This type of energy would exhibit exactly the right type of behavior, except for one thing: Based on the standard model, the hypothesized energy density appears too large by at least 100 orders of magnitude. While it is technically possible for as-yet-undiscovered quantum fields to yield a partial cancellation, the cancellation would have to yield a result so miraculously close to zero that many view the vacuum energy as a mathematical oddity and not a viable cosmic force. Still, it is clear that physics is missing something here.

Lastly, a more tangible problem in the standard model is that of neutrino mass. Neutrinos are observed to have a miniscule mass relative to all other particles. Yet they have no mass term at all in the standard model, and one cannot be added in quite the same way as for other fermions, because neutrinos seem to exist only as left-handed particles. One interesting possibility is the see-saw mechanism, which posits that right-handed neutrinos do in fact exist and are very heavy, making them possible candidates for dark matter. However, there are other possibilities as well.

2.2 Quantum Fields: rough around the edges

We alluded in Chapter 1 to the fact that QFT is rather messy from a mathematical standpoint. In QFT, true quantum field interactions involve arbitrarily complex diagrams which often cannot be calculated even with today's computing resources. On top of that, most Feynman diagrams hide integrals that yield infinite results upon first attempt to caulculate anything physical. They must be be put through a process called *renormalization*, whereby physical quantities are redefined specifically to avoid divergent quantities. While the process of renormalization has had great success in making physical predictions, and the formulation of the renormalization group approach by Wilson in the 1970s [15] sheds some additional light on the once-controversial process, it has one fundamental issue: it is not mathematically rigorous. This is not a deal-breaker, as Newton's calculus was wildly successful for over a century before being made fully rigorous by mathematicians. Nevertheless, it sets an obvious direction for needed mathematical work.

While the process of renormalization can be quite technical, the conceptual issue is simpler: renormalization is used to answer a question in physics when the original phrasing of the question, resulting from the equations in QFT, has no apparent solution. Renormalization requires one to redefine the quantities in the problem until divergences cancel and a finite result can be obtained. This redefinition means that the original question has not been answered in a strict sense, creating an ambiguous divide between the equations of the theory and the results of the theory. For an excellent discussion on the concept of renormalization in a broad sense, see Arnab Kar's dissertation [16].

Such an issue is not so different from Newton's use of *infinitessimals* in his formulation of calculus–these objects were not defined in a mathematically rigorous way, but were used to produce many results nonetheless. However, they start to come up short when one starts to push calculus to its extreme limits, studying functions that appear bizzare and physically unintuitive. Unfortunately, most objects in QFT are bizzare and physically unintuitive, suggesting that they may benefit from more rigorous mathematical formulation.

Recently, some work has been done in the direction of making mathematically rigorous the renormalized solutions to certain field theories. Notable work has been done by mathematicians working in the language of stochastic calculus, such Martin Hairer's work on regularity structures in 3-dimensional $\lambda\phi^4$ theories. One can find an overview of Hairer's novel approach in Ref. [17].

Because there are situations where renormalization breaks down (strongly-coupled theories and gravity to name a few), it will ultimately be important to have a rigorous understanding of the procedure so we may better understand its limits.

2.3 The strongly coupled regime

Despite the caveats of perturbative expansion and renormalization, those procedures take place under conditions under which QFT is still able to thrive. The theory succeeds when the interaction coupling strength is small, as the perturbative approach of Feynman diagrams and renormalization converges quickly. The contributions of diagrams die off as they become more and more complex. But this is not always the case, particularly for the strong interaction.

All interactions in QFT have what is called a *running coupling*–as a consequence of renormalization, the apparent strength of the interaction varies as a function of energy/length scale. In the case of the strong interaction, the coupling is small at very high energies, allowing us to predict the results of high energy particle collisions involving quarks and gluons. However, the coupling becomes large at low energies, causing quarks to join together and *hadronize* into bound states. QFT, for all its success, struggles to demonstrate exactly how quarks form bound states, or to explain why the proton mass is so much higher than its constituent valence quarks. Some success has been seen in modelling these non-perturbative effects numerically through lattice field theories, for example in calculating meson masses (see Ref. [18] for a review).

Lattice QCD, coupled with observations and effective field theories, is generally seen as sufficient evidence for the validity of QCD and the quark model. Nonetheless, the inability to make calculations involving real world particles based on first principles is noteworthy. From a purely mathematical standpoint, the strongly coupled regime eludes description by tools. This leaves open the meaning of other hypothesized field theories which become strongly coupled at high energies–can such a theory exist in nature? QED was thought to be such a theory before EW unification, but the additional symmetry group sieved divergences at high energy scales.

To this day, understanding the low energy behavior of QCD directly ties into one of the famous Millenium Problems [19], so you could win $\$1,000,000$ if you figure it out! The problem in question is to demonstrate that non-abelian gauge theories called Yang-Mills theories, which include QCD, have a mass gap. In QCD, this would mean that gluons are somewhat a ruse, existing only as virtual particles in perturbative diagrams at high energies. All *real* excitations of the gluon field would have to be a bound state of many constituents which acquires a mass.

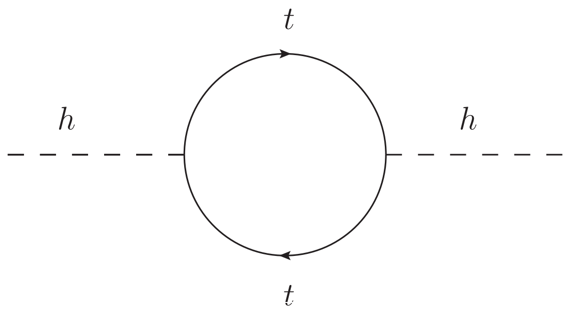

Figure 2.1: A diagram for a top quark loop correction to the Higgs propagator, which will affect the Higgs mass renormalization. Because the Higgs boson couples to all massive fermions, it is influenced by many such diagrams.

2.4 The hierarchy problem

The hierarchy problem can be stated in a few ways. First, we note that at present there is only one independent parameter in the SM which is not dimensionless in natural units: essentially, the Higgs mass. The mass of the Higgs boson sets the energy scale for the electroweak interaction, and arguably for much of the standard model, though we are ignoring a more subtle scale that arises in QCD here. Quantum Gravity should have a natural scale on the order of the Planck mass m_{pl}, 16 orders of magnitude larger than the Higgs mass. What can explain this enormous difference? In one sense, this question itself constitutes what is referred to as the hierarchy problem. in another sense, there is a more specific issue at play.

The hierarchy problem can also be more technically posed in terms of the Higgs mass renormalization. The trouble comes from the fact that the Higgs couples to other particles via loop diagrams, as in Figure **??**. Such diagrams must be included in the Higgs mass renormalization, and their contribution depends on the mass squared of the particle appearing in the loop. This means that any heavier particles we have not yet observed ought to produce large corrections to the Higgs mass. Indeed, if there exist new physics at energies much higher than the EW scale (which the Planck mass strongly suggests), it seems impossible that the Higgs mass would remain comfortably within the EW regime, as an extreme fine-tuning is needed to balance the larger and larger loop corrections. Such fine-tuning is detested by particle physicists. In general, it seems possible for nature to possess terms at different scales that bear little relation, and also for many exact cancellations. However, incredibly unlikely *approximate* cancellations are frowned upon without a good explanation.

The favored resolution to this problem has been supersymmetric (SUSY) models, in which the additional particles create a cancellation effect above the SUSY energy scale, removing the need for fine-tuning. However, with no direct evidence of SUSY, the potential energy scale for SUSY has been pushed ever higher, while the measured Higgs mass that fits comfortably with current SM data. It is not clear how new physics could come eventually come into play at higher energies without greatly effecting the Higgs mass, unless these effects are wildly different than the particle interactions we understand today.

honorable mentions

We pause here to note a few more mysteries of the standard model that may pique the interest of some readers: There is the strong CP problem [20], in which a viable CP-violating term is conspicuously absent from the QCD Lagrangian, a fact that has been used to conjecture about hypothetical particles called axions. Another fundamental problem is the discrepancy between observed CP violation in the standard model and matter anti-matter asymmetry in the visible universe [21], which seem incompatible. Lastly, for those interested in early universe cosmology, the lack of a plausible bridge between the standard model and the model of inflationary cosmology remains an open and intriguing issue [22].

Chapter 3

Theoretical paths forward

UNDER CONSTRUCTION

Chapter 4

Experimental paths forward

4.1 The energy frontier

The most obvious path forwards is to build higher and higher energy colliders and see what happens. Particle physics research which takes place at this energy frontier is often called *high energy physics*, a name which helps to set it apart from other types of particle physics experiment which do not rely on enormous colliders. The Large Hadron Collider (LHC), discussed further in Chapter 6, is currently the highest energy collider ever built, and is firmly at the epicenter of experimental high energy physics today.

It is a guarantee that new physics will emerge eventually, but the energy at which this will occur has become unclear since the discovery of the Higgs boson in 2012. This is a fairly new situation–prior to the 2012, there were widely accepted arguments that if the Higgs boson were not found in its expected mass range, some other new physics would be found around the same energy energy scale. But in

2020, there are currently no easily accessible energy ranges which have an obvious need for new physics. Models for extra particles and dark matter candidates often have many free parameters that cause them to become relevant at arbitrary energy scales.

Although discovering new particles is perhaps the most exciting and glamorous way to advance experimental high energy physics, it is not the only path forward, and seems increasingly unlikely in the near future of the field. The lack of a clear direction for high energy experimental physics pushes us towards an era of precision measurement, in which every aspect of the existing model and data is pored over extensively.

Previously, precision measurements have pointed the way to new physics well in advance of direct discoveries. For example, the mass of the top quark was predicted in advance of its discovery by precision fitting in the electroweak sector of the standard model [23]. It is possible that future data-taking at the LHC and the planned upgrade to HL-LHC will yield precision results that suggest new physics. However, particle physics at the energy frontier is today a bit more directionless than in the 1990s–we do not expect to find heavier quarks or a long-missing scalar boson. We know that something is missing from the existing model, but we can’t agree what.

4.2 Other approaches

Before proceeding into our experimental research, we note briefly for the reader other exciting avenues of physics research which can crack away at the fundamental questions addressed in this document.

Neutrino experiments are making slow but steady progress in illuminating the properties of these often invisible particles. For example, shortly before the writing of this dissertation, the T2K experiment in Japan published a result regarding the constraint of CP violation occurring via neutrino oscillation [24]. Arguably, neutrinos are the only particles currently measured to disobey the standard model, because they have mass (albeit very little). In the minimal formulation of the standard model, they are massless. While adding in neutrino mass does not exactly shatter the standard model into pieces, there is some ambiguity on what mechanism gives rise to it, and whether they may have heavy unobserved counterparts.

Neutrinos are difficult to detect, and generally we must have trillions of neutrinos pass through large liquid-filled detectors to observe even a few. Otherwise, they simply pass right through everything they encounter. There are many interesting experiments which are either collecting data now or will begin in the near future, such as the T2K experiment in Japan and the DUNE collaboration in North America. These have the potential to revise our understanding of the standard model in the coming decades. In a completely different approach to study neutrinos, there are also experimental searches for neutrino-less double beta decay, which could determine if neutrinos are Majorana fermions and shed light on the problem of neutrino mass. Overall, this sector of research tends to generate results at a reliable, steady pace.

Dark matter searches are experiments which try to detect signs of dark matter. Direct detection experiments can be large tanks of liquid underground, similar to neutrino detectors, hoping to detect the signature of a new particle passing through. There are also indirect detection experiments–for example, those that search for decay products of dark matter annihilation in outer space. Relative to the slow and steady trickle of information from neutrino experiments, this sector is a bit of a lottery. At any time, one of them could detect the signature of a dark matter candidate, completely upending the world of particle physics and surely meriting a Nobel Prize.

Cosmological experiments are closely linked to particle physics as well–the standard model governs much of the way the early universe behaved. Thus, measurements of the cosmic microwave background, and perhaps someday the cosmological gravitational wave background, can have profound implications for dark matter models and particle physics in general.

These are just a few to highlight the breadth of experimental approaches that could shed light on the fundamental mysteries of particle physics. There are many others, from searches for magnetic monopoles, to cosmic ray detection, to antimatter confinement studies, to precision studies of radioactive decay... As the rate of new discoveries from the energy frontier slows, perhaps the next big breakthrough in particle physics will come from a new type of experiment which generates little excitement today.

Chapter 5

Top quarks and collider physics

Why are top quarks interesting?

The top quark is the heaviest known fundamental particle at the time of this dissertation's writing. It has a measured mass of 172.4 GeV, a bit higher than the Higgs boson mass of 125 GeV. This makes its mass 40 times higher than that of the next heaviest quark, and over 300,000 times heavier than that of an electron. Recalling the mass-Yukawa relationship from section 1.8, we see that the top-Higgs Yukawa coupling, g_t, is within a few percent of $g_t = 1$. Given that the value is completely arbitrary in the standard model, one might consider it a bit suspicious–especially in relation to other fermion Yukawa coupling strengths, which are orders of magnitude lower. Additionally, its heavy mass makes the top quark highly unstable, making it the only quark to decay prior to hadronization. This opens up an experimental window into fundamental physics interactions at the highest energies

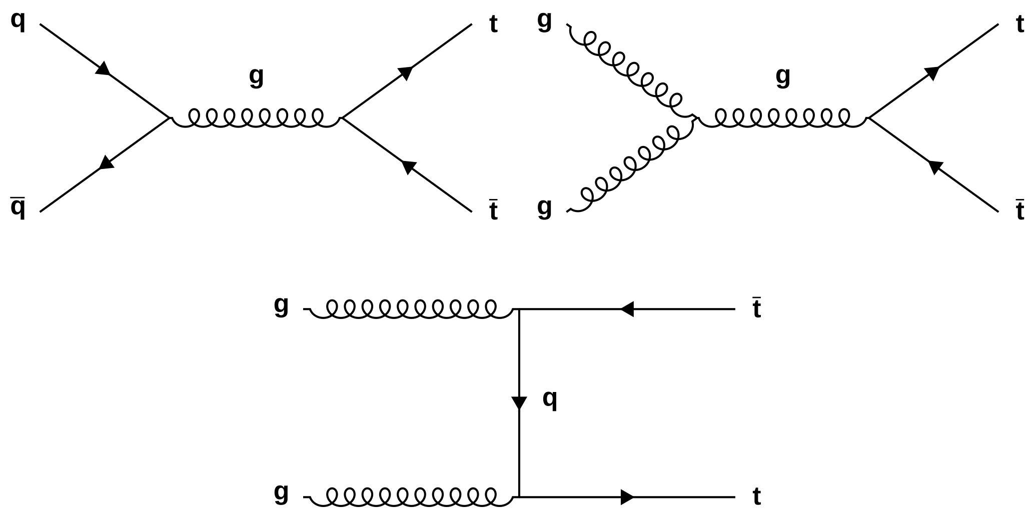

Figure 5.1: Example diagrams for leading order $t\bar{t}$ production via qq and gg processes.

currently attainable, making the top quark one of the most useful tools to advance our understanding of the standard model.

5.1 Top production at hadron colliders

For the purposes of this document, we will focus on top quarks produced as quark anti-quark pairs. Top quark pair production, or $t\bar{t}$ production for short, occurs when a top and anti-top quark are produced together in an inelastic collision. At hadron colliders, this happens mostly due to strong interactions between quarks and gluons, as shown in Figure 5.1. Pair production is generally the easiest way to observe top quarks, and served as the initial means of discovery for the top quark at the D∅ and CDF experiments in 1995 [25,26].

At colliders, the starting point for QFT calculations is a scattering *cross section* σ. As the name might suggest, this has dimensions of area, and is often expressed in terms of the unit Barns $\mathrm{b} = 10^{28}\,\mathrm{m}^2$. In classical theory, a scattering cross section is the size of the area perpendicular to two particle's motion within which they must pass to interact and scatter. In quantum theory, it is related to the probability that two initial state particles interact and product a given final state. For example, from 2016–2018 the CMS experiment recorded an integrated luminosity of about $L_{\mathrm{tot}} = 137\,\mathrm{fb}^{-1}$ of collision data. The total cross setcion for $\mathrm{t\bar{t}}$ production from proton-proton collision at the appropriate energy is calculated to be about $\sigma_{\mathrm{pp}\rightarrow\mathrm{t\bar{t}}} = 840\,\mathrm{pb}$ [27]. Multiplying the two, we can estimate that the number of top quark pairs produced and recorded at the CMS detector during this period was about $L_{\mathrm{tot}} \times \sigma_{\mathrm{pp}\rightarrow\mathrm{t\bar{t}}} = N_{\mathrm{t\bar{t}}} \approx 10^8$ events.

The basic relationship between Feynman diagrams and and cross sections will be important. While we won't calculate any in this dissertation, Feynman diagrams stand in for integrals used to calculate elements in a perturbative expansion of the scattering matrix. Each vertex of a Feynman diagram carries a factor relating to the coupling constant governing the relevant interaction, such as α_{s} for QCD diagrams in Fig. 5.1. The associated *matrix element* $\mathcal{M}_{i\rightarrow f}$, for initial state i and final state f, carries a factor of $\sqrt{\alpha_s}$ for each vertex in the diagram. The cross section follows the relationship

$$d\sigma \propto |\ \mathcal{M}_{i\rightarrow f}\ |^2, \tag{5.1}$$

and so cross section calculations themselves effectively carry one factor of the coupling α_s for each vertex (though things can get more subtle when summing over initial and final states).

Thus, the diagrams in Fig. 5.1 are said to be of order $\mathcal{O}(\alpha_s^2)$, which is the leading order (LO) $t\bar{t}$ production. Diagrams of order $\mathcal{O}(\alpha_s^3)$ are then next-to-leading order (NLO) QCD diagrams, and so on. These higher order diagrams can contain either loops of virtual particles, or emissions of additional real particles in the final state.

One can also calculate *differential cross-sections*, to look at the relative probability of final states as a function of some kinematic variable. This will tell you how many events to expect as a function of the desired variable. For example, we will be looking at the differential $t\bar{t}$ cross section with respect to the invariant mass of the $t\bar{t}$ system, $d\sigma_{t\bar{t}}/dM_{t\bar{t}}$. We show a theoretical result for this differential cross section in Fig. 5.2. We see that pair production begins at threshold mass of $2m_t \approx 345\,\text{GeV}$ and peaks slightly after, trailing off at higher values of $M_{t\bar{t}}$.

5.2 Top quarks: decay and detection

Top pair production has a relatively high cross section and leaves unique byproducts which are easy to distinguish from other processes. When they are produced, top quarks have an incredibly short lifetime of about 10^{-25} seconds. Because of this short lifetime, the top quark is the only quark which decays via a fundamental Feynman vertex modeled by perturbative calculations. In the standard model, top quarks decay almost exclusively to a bottom (b) quark and a W-boson, with a branching fraction of over 99%. We briefly discuss each byproduct.

The **b quark** survives long enough to hadronize, generally forming a B hadron. This hadron then typically travels a distance on the order of several millimeters before decaying at a secondary vertex. Like other quarks and unstable particles,

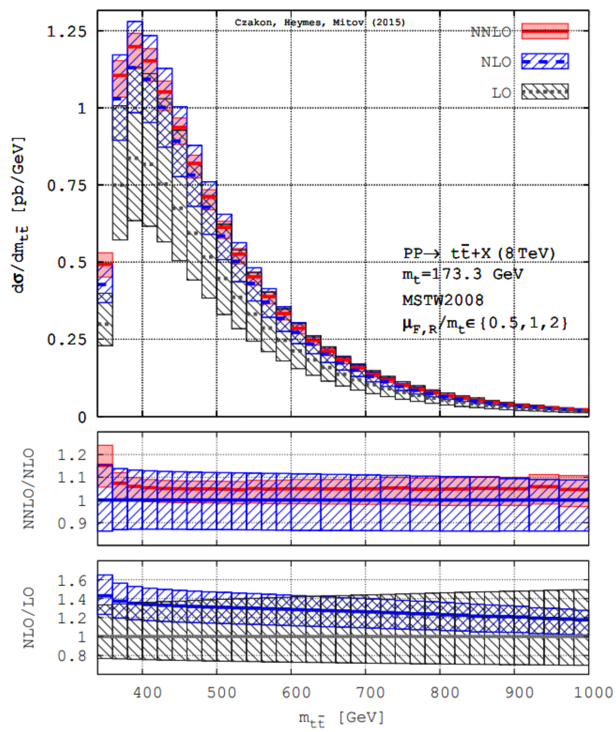

Figure 5.2: Fixed-order theory calculations of $d\sigma_{t\bar{t}}/dM_{t\bar{t}}$ are shown at LO, NLO, and NNLO in QCD for proton-proton collisions at $\sqrt{s} = 8\,\text{TeV}$ and a top mass of $m_t = 173.3\,\text{GeV}$. This figure is taken from Ref. [1] by Czakon, Mitov, and Heymes. Uncertainty bands are based on varying the renormalization and factorization scales, μ_r and μ_f, respectively.

the b quark is ultimately detected as a shower of particles called a jet. Luckily, Information about particles which appear to come from secondary vertices, together with additional jet kinematics, can be used to distinguish b jets from other jets with reasonable success [28]. Different algorithms and working points are available to identify b jets, which have varying rates of sensitivity (the rate of correct identification fraction of b jets) and specificity (the rate of mis-identification of other jets). $\mathrm{t\bar{t}}$ decays benefit from having two associated b-jets, which helps greatly in distinguishing them from other physics processes.

The **W boson** has two options for decay. First, it can decay *hadronically* into a quark anti-quark pair, which both hadronize and are in practice detected as one or two jets. Secondly, it can decay *leptonically* into a lepton and neutrino pair. If the lepton is an electron (e) or muon (μ), it can be detected and reconstructed. Tauons (τ) decay quickly and can sometimes be reconstructed by their decay products, though many measurements try to avoid events with taus due to the added challenge. Meanwhile, the neutrino (ν) escapes undetected, leading to an imbalance in transverse momentum with respect to the beam axis which contributes to $\boldsymbol{p}_{\mathrm{T}}^{\mathrm{miss}}$. While this presents a challenge in reconstructing the neutrino momentum, it also offers another way of distinguishing $\mathrm{t\bar{t}}$ events, as they will generally have a large value for $p_{\mathrm{T}}^{\mathrm{miss}}$.

The process of identifying $\mathrm{t\bar{t}}$ decays is helped by the fact that these decay products will generally have high p_{T} relative to decays of many other physics processes. The channel with the lowest background rate is the dilepton final state, where both W bosons decay leptonically. The presence of two b jets, two high p_{T} leptons, and large $p_{\mathrm{T}}^{\mathrm{miss}}$ makes it easy to distinguish these events and obtain samples of high purity. However, it does have lower statistics than the other decay channels, with a branching fraction of only 11% in $t\bar{t}$ decays.

Because of the high purity and relatively high cross section, $t\bar{t}$ events offer a unique ability to measure differential cross sections with high precision. We will see in chapter 7 how the shape of such measurements can be used to study the interaction of top quarks with other particles.

5.3 $t\bar{t}$ simulation at CMS

Simulation of top quark pair production at CMS begins with a NLO QCD matrix element computation, using the POWHEG generator [29–32]. This calculation is performed with the renormalization μ_r and factorization scale μ_f set to the transverse top mass, $m_T = \sqrt{m_t^2 + {p_T}^2}$. A top quark mass of $m_t = 172.5\,\text{GeV}$ is used in all simulations. The matrix element calculations obtained from POWHEG are then matched with parton shower (PS) simulation from PYTHIA8 [33–35]. Pythia uses the underlying event tune M2T4 [36] in 2016 and the CP5 tune in 2017 and 2018 [37]. The parton distribution functions from NNPDF3.0 at NLO [38] are used in 2016 and updated to NNPDF3.1 [39] at next-to-NLO (NNLO) in 2017 and 2018. In the near future, samples will be available which update the simulation in 2016 to match the other years, but these are not available at the time of this document's writing.

We note here a few fundamental sources of uncertainty in the modeling. First, the scales μ_r and μ_f are varied up and down by a factor of 2 to obtain a rough model of uncertainty coming from higher order QCD terms in the matrix element

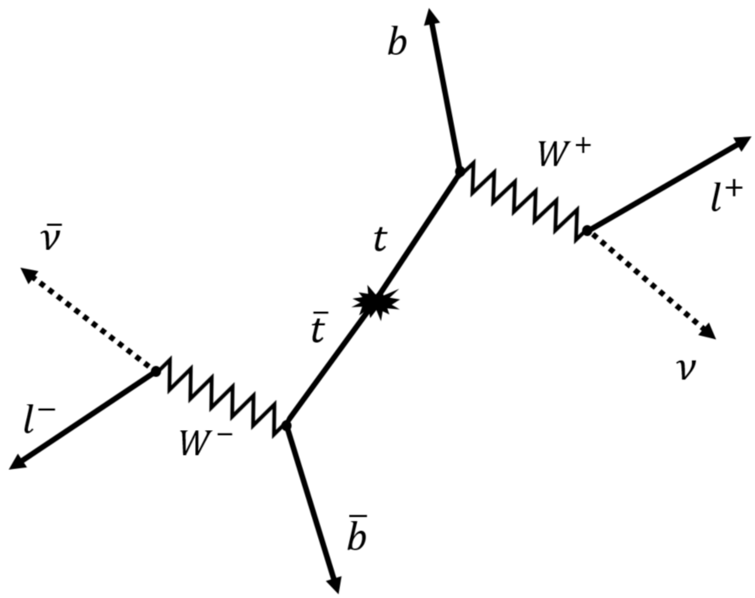

Figure 5.3: top pair production decaying into the dilepton final state

calculation. This is a standard practice in assessing uncertainty on perturbative QFT calculations, as dependence on scale choice is an artifact of the perturbative approximation. The variation by factor of two is rather arbitrary, but frequently performs well and has become a rule of thumb in the field.

The scale is also varied in the parton shower algorithm, performed separately to assess both the uncertainty on initial state radiation (ISR) and final state radiation (FSR). Finally, the makers of the NNPDF sets provide variations which model the uncertainty on the underlying parton distribution functions.

5.4 Kinematics of dilepton event reconstruction

The process of two top quarks each decaying leptonically is visualized in Fig. **??**. The two undetected final state neutrinos create a challenge in reconstructing the top quark kinematics. However, if one forces the decays to be strictly on-shell, meaning that 4-momentum is exactly conserved at each vertex and the mass width of t and W are ignored, the neutrino momenta can be in theory determined exactly.

Specifically, for each top quark decay, conservation of energy E and momentum $\vec{p}$ at each vertex yield

$$E_\mathrm{t} = E_\mathrm{b} + E_\mathrm{W} = E_\mathrm{b} + E_\ell + E_\nu, \tag{5.2}$$

$$\boldsymbol{p}_\mathrm{t} = \boldsymbol{p}_\mathrm{b} + \boldsymbol{p}_\mathrm{W} = \boldsymbol{p}_\mathrm{b} + \boldsymbol{p}_\ell + \boldsymbol{p}_\nu. \tag{5.3}$$

The momenta $\boldsymbol{p}_\mathrm{b}$ and $\boldsymbol{p}_\ell$ and the corresponding energies are known from measurement. The masses of the top quark and W boson are taken as fixed, entering through the quadratic relationship

$$E^2 = \mid \boldsymbol{p} \mid^2 + m^2. \tag{5.4}$$

With the neutrino's mass taken to be zero, each vertex of the decay generates a set of quadratic equations which constrain $\boldsymbol{p}_\nu$ to an ellipsoid in 3-dimensional momentum space (5.4 left). The neutrino momentum is thus constrained to lie on the intersection of these two surfaces, which traces out an ellipse. We call this the *mass constraint*, and it is not always possible to satisfy, as the two ellipsoids will not generically intersect. Occasionally, this is due to small deviations from the on-shell assumption (recalling that intermediate particles are virtual), or from measurement resolution. More commonly in practice, it occurs in the case of an incorrect event reconstruction where a jet has been mis-identified or placed at the wrong vertex.

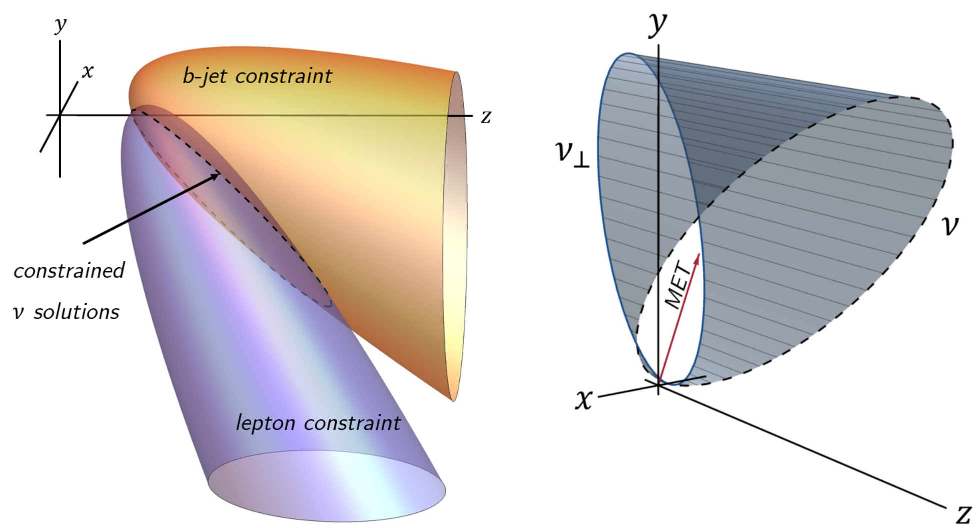

Figure 5.4: Left: ellipsoidal constraints on neutrino momentum, whose intersection defines an ellipse. Right: The elliptic constraint projected into the transverse plane.

If the mass constraint can be formed, this ellipse can then be projected into the transverse plane to define a constraining curve $\boldsymbol{\nu}_\perp$, which can be related to the measured quantity $\boldsymbol{p}_\mathrm{T}^\mathrm{miss}$ (also known as the MET vector). In the case of semi-leptonic decays, with only one undetected neutrino, we can simply introduce a parametrization $\boldsymbol{\nu}_\perp(\theta) : [0, 2\pi] \mapsto \mathbb{R}^2$ and find the point $\boldsymbol{\nu}_\perp(\theta)$ which minimizes the distance to $\boldsymbol{p}_\mathrm{T}^\mathrm{miss}$.

In dilepton decays, with two final state neutrinos carrying away undetected momentum, we must repeat this argument twice. This results in two separate transverse momentum constraints, $\boldsymbol{\nu}_\perp$ and $\bar{\boldsymbol{\nu}}_\perp$ (Figure 5.5). We wish to find points on these two ellipses, specified by parameters θ_1 and θ_2, such that

$$\boldsymbol{\nu}_\perp(\theta_1) + \bar{\boldsymbol{\nu}}_\perp(\theta_2) = \boldsymbol{p}_\mathrm{T}^\mathrm{miss} \tag{5.5}$$

This can be rewritten as

$$\boldsymbol{\nu}_\perp(\theta_1) = -\bar{\boldsymbol{\nu}}'_\perp(\theta_2) \tag{5.6}$$

where $\bar{\boldsymbol{\nu}}'_\perp(\theta_2) \equiv \boldsymbol{p}_{\mathrm{T}}^{\mathrm{miss}} - \bar{\boldsymbol{\nu}}_\perp(\theta_2)$. This new ellipse maintains the overall shape of $\bar{\boldsymbol{\nu}}_\perp$, but is shifted and rotated 180° about its center. The problem then reduces to the intersection of two ellipses. We call this the *MET constraint*. The MET constraint can be satisfied if the two ellipses do intersect, which will yield a discrete set of either 2 or 4 possible momenta for the neutrinos. Because the MET is a difficult quantity to measure in practice, it is not infrequent that the MET constraint cannot be exactly satisfied even if the other objects in the event were correctly identified and well reconstructed. In this case, an approximate solution can be taken from the points of closest approach of the two ellipses.

The full kinematic reconstruction was not used for the final measurement presented in Chapter 7, but the kinematic constraints outlined here are still used to aid in determining which b-jets and leptons are likely to originate from the same top quark. We show in Figure 5.6 how, in simulated events, the results of the two kinematic constraints when comparing correct and incorrect matching of b jets to leptons. This emphasizes the role of these kinematic constraints as a tool to aid with proper selection and assignment of b-jets.

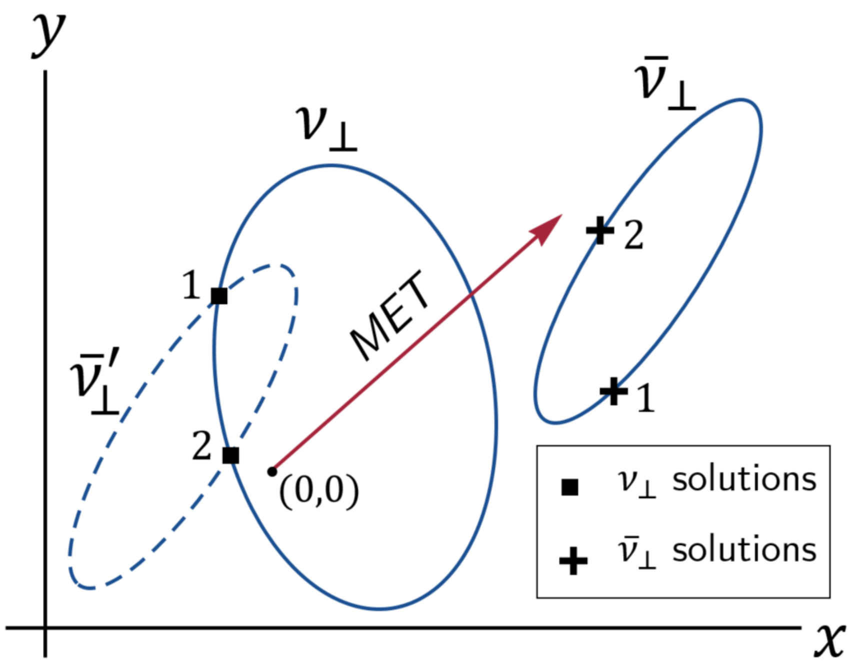

Figure 5.5: combination of 2 ellipses in the dilepton case

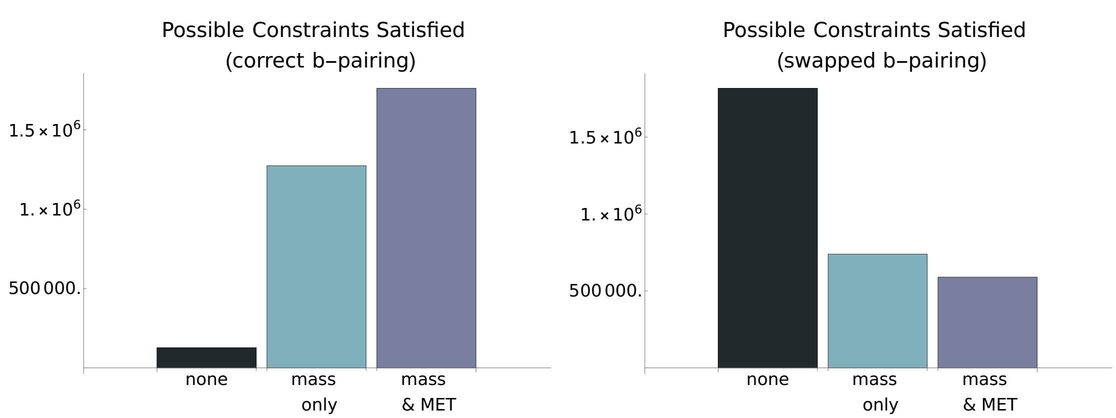

Figure 5.6: We show the frequency with which the different kinematic constraints can be satisfied, comparing the case where the two b jets are paired with the correct leptons against the case where they are not.

Chapter 6

The CMS Experiment

6.1 The Large Hadron Collider (LHC) apparatus

The LHC [40] is the largest and highest-energy particle collider ever constructed, spanning across the border of France and Switzerland near the city of Geneva. The main ring, which uses the tunnel from the Large Electron Positron collider (active 1989-2000), has a diameter of 8.6 km and ranges from 50-175m underground along its circumference. Its primary function is to store and collide circulating beams of protons at energies of up to 14 TeV, though it is also used to collide heavy nuclei during limited data-taking periods. Particle energies are ramped up with a series of smaller linear and circular accelerators before entering the main ring. In this document, we will discuss the machine from the proton-proton collision perspective; for more on the physics resulting from heavy ion collisions at the LHC, see for example the review [41].

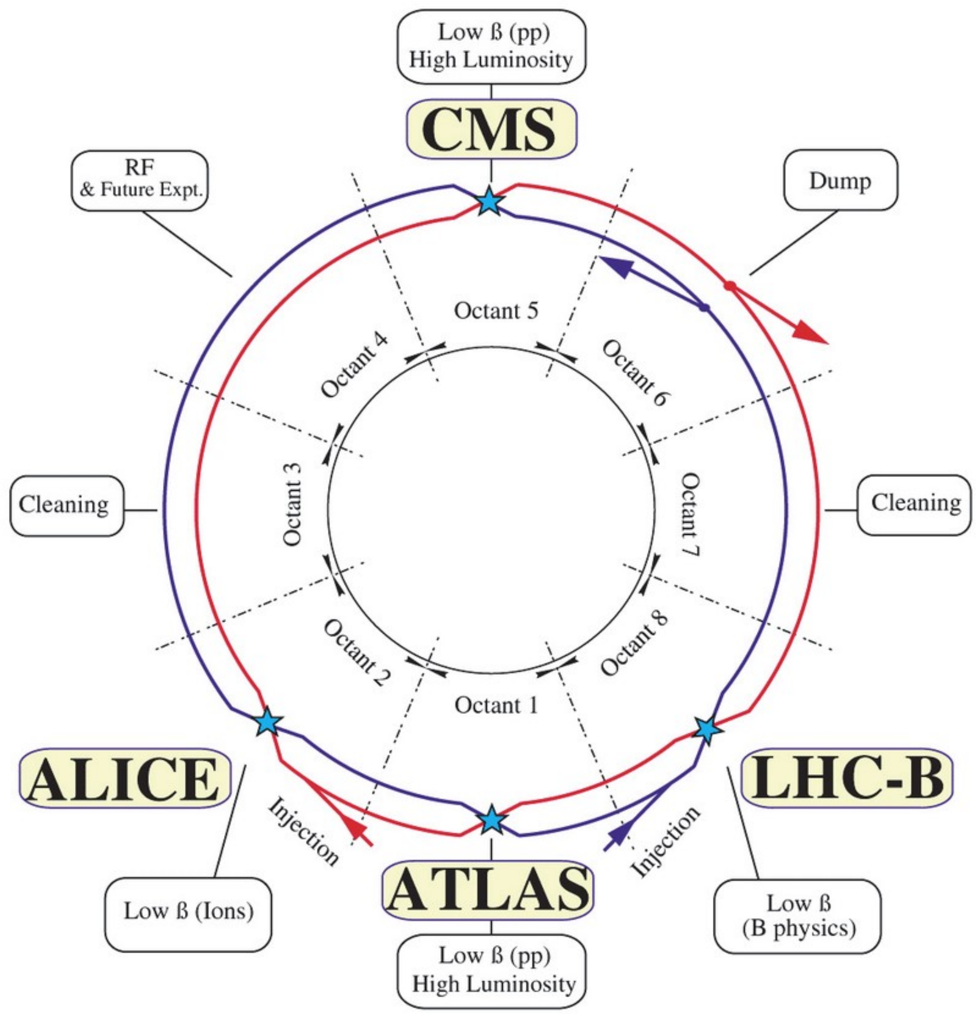

Figure 6.1: A map showing the layout of LHC. The primary experiment at each of the 4 bunch crossings is labeled, but there are also smaller experiments associated with these points.

Protons circulating in the LHC ring are divided into bunches prior to injection. Each bunch contains around 10^{11} protons and is about 30cm long (from the laboratory reference frame). The main ring has over 2000 bunches circulating simultaneously when running at its current beam capacity.

There are several experiments designed to detect results of collisions at 4 beam crossing points, shown in Figure 6.1. Of these detector experiments, the two largest are the CMS and ATLAS experiments, both of which are general purpose detectors aimed at measuring and reconstructing a broad range of collision byproducts and outcomes. CMS is an acronym for *Compact Muon Solenoid*, while ATLAS supposedly results somehow from the words *A Toroidal LHC Apparatus* (though many scientists believe that this shortening violates the fundamental rules of an acronym).

The LHC was first turned on in 2008. The first data-taking run for experiments took place from 2010-2013, where collisions took place at an center of mass energy of 7 to 8 TeV. After a long shutdown for upgrades and maintenance, the beam energy was increased to 13 TeV for the second run of data taking, which took place from 2015-2018. In particle physics, the center of mass energy (total energy of the colliding protons in the rest frame) is denoted by $\sqrt{s}$, due to its relationship to the traditional mandelstam variable s.

6.2 The CMS detector

The detector has 5 main layers, consisting of 4 types of detectors and the solenoid magnet which is the experiment's namesake, as shown in Figures 6.2-6.3. We briefly outline the detector components here, from innermost to outermost.

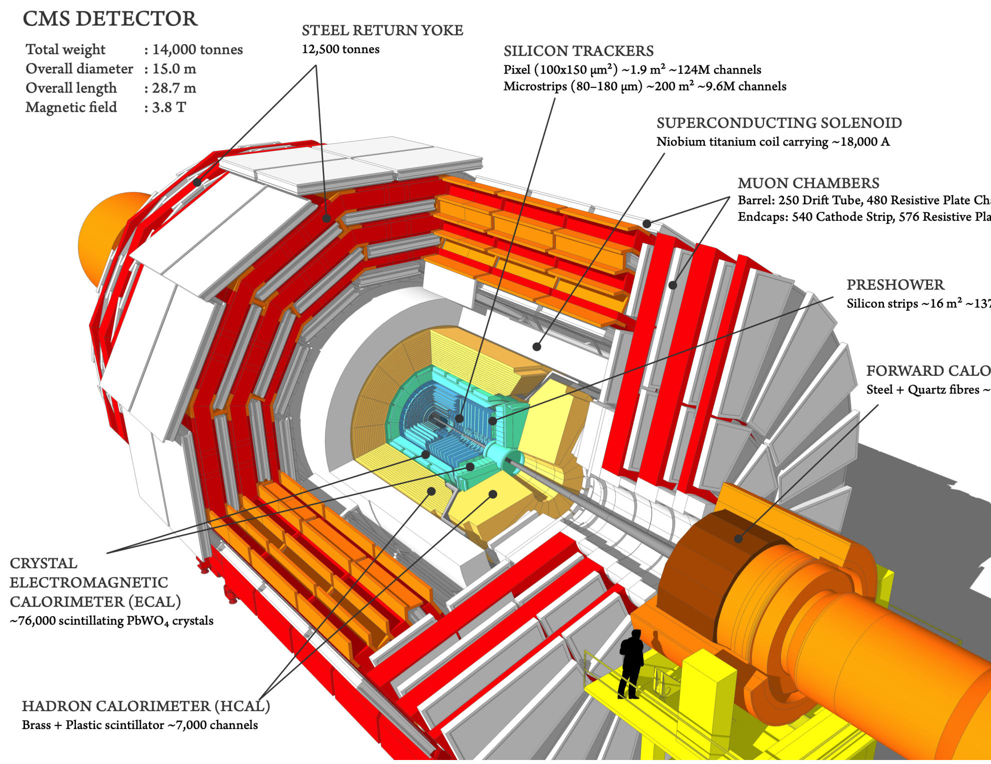

Figure 6.2: a 3-dimensional rendering of the CMS detector is shown, indicating the scale of the detector and the overall layout of the internal components with respect to the beam pipe.

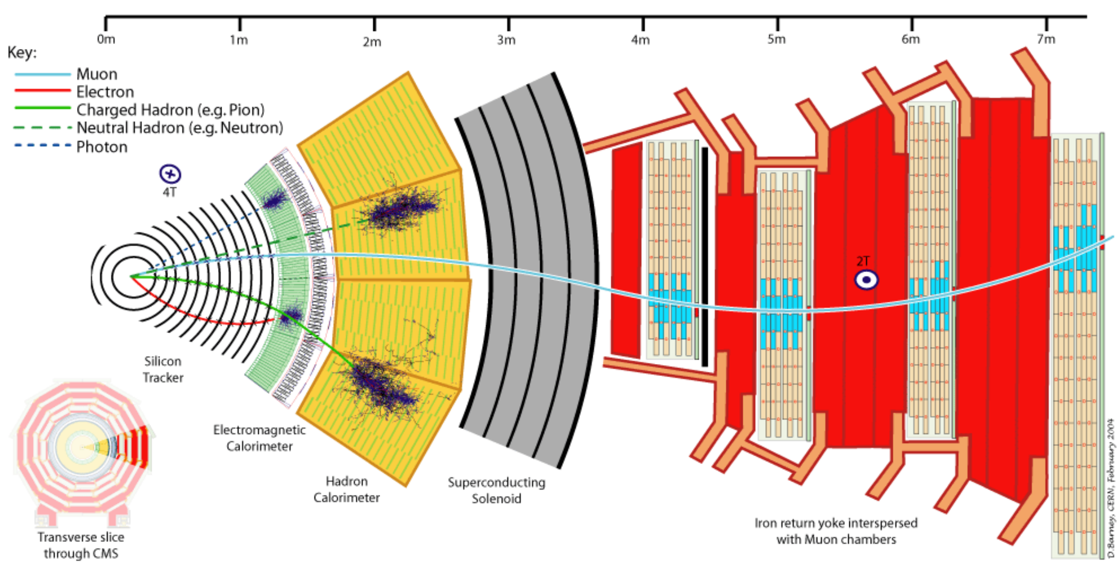

Figure 6.3: A cross sectional slice of the CMS detector is shown with example particle tracks demonstrating the function of each detector layer

1. The **tracker** is comprised of an inner portion with high-granularity silicon pixels and an outer level of silicon strips. A particle passing through the silicon material will create loose electron/hole pairs. A reverse bias voltage generates an electric field which prevents these pairs from recombining, and they drift through the bulk of the material to readout sensors where the effect can be detected.

   With the many layers of silicon pixels and strips, we can reconstruct precisely particle trajectories. Due to the presence of a strong magnetic field, these trajectories will be curved, and the charge-to-mass ratio of particles can be estimated. The silicon tracker is essential for estimating the location of the vertex at which particles are produced, which may be displaced from the primary vertex of a collision. This is essential in b-jet identification, for example.

2. The **electromagnetic calorimeter** (ECAL) consists of a dense material which detects electrons and photons, causing them to decay into a well-defined burst/shower of particles. The energy deposited by this burst can be measured and used to estimate the energy of detected particles. As the electromagnetic interaction scales like $1/m^2$ for particles with mass m, heavier particles like hadrons/mesons and muons can pass through this layer with minimal disturbance.

3. The **hadronic calorimeter** (HCAL) is another calorimeter designed to detect hadrons/mesons. It can detect charged and neutral particles of this type. Among standard model particles, only muons and neutrinos can easily pass through this layer undisturbed.

4. The **superconducting solenoid** (magnet) is the largest magnet of its kind ever constructed, producing magnetic field strengths of up to 3.8 T. This strong magnetic field causes the paths of charged particles to curve based on their mass and velocity, aiding greatly in particle identification and reconstruction. This is arguably the central design element of the detector and its namesake.

5. The **muon detector** detects only muons, and also contains several layers of iron return yoke to ensure that any particles other than muons are blocked before entering this region (excluding neutrinos). While the muons pass easily through all solid components of CMS, the muon detector primarily uses small gas chambers to detect them. The muons will knock electrons off of particles in the gas, creating a detectable signal. Though the spatial resolution of this type of detector is worse than others, the muons are detected at several locations and are the most easily identified particle, making them the cleanest data points in most collisions. The magnet allows their velocity to be easily computed by the observed radius of curvature of their flight path.

The particle-flow (PF) algorithm [42] aims to reconstruct and identify each individual particle in an event, with an optimized combination of information from the various elements of the CMS detector. The energy of photons is obtained from the ECAL measurement. The energy of electrons is determined from a combination of the electron momentum at the primary interaction vertex as determined by the tracker, the energy of the corresponding ECAL cluster, and the energy sum of all bremsstrahlung photons spatially compatible with originating from the electron track. The energy of muons is obtained from the curvature of the corresponding track. The energy of charged hadrons is determined from a combination of their momentum measured in the tracker and the matching ECAL and HCAL energy deposits, corrected for zero-suppression effects and for the response function of the calorimeters to hadronic showers. Finally, the energy of neutral hadrons is obtained from the corresponding corrected ECAL and HCAL energies. A more detailed description of the CMS detector can be found in [43].

The standard coordinate frame uses the z-axis as the beam axis, while the x-axis points inwards towards the center of the ring and the y-axis points vertically upward. The $x - y$ plane is referred to as the transverse plane, and projections of momenta p into this plane are labeled p_{T}. Conservation of momentum dictates that a collision should produce no net momentum in this plane.

The pseudo-rapidity η is frequently used in discussing particle kinematics, as it is closely related to the polar angle θ measured from the beam axis by the formula $\eta = -\ln(\tan(\theta/2))$. Notably, the tracker covers the angular range $\mid \eta \mid < 2.5$ (Fig. 6.4), while the muon detector covers $\mid \eta \mid < 2.4$ (Fig. 6.5). Though some specialized forward calorimeters allow some detection of particles up to $\mid \eta \mid < 5$, high-quality reconstruction is generally restricted to objects within the tracker/muon detector coverage.

6.3 Collision basics

Though the LHC generates proton-proton collisions, protons are not the most fundamental participants in the inelastic collisions which produce exotic states of matter. Recall that protons are a bound state of 3 quarks, called the *valence quarks* quarks. Due to the strongly coupled nature of QCD interactions, this bound state is less of an inanimate collection of 3 stable ingredients, and more of a living organism

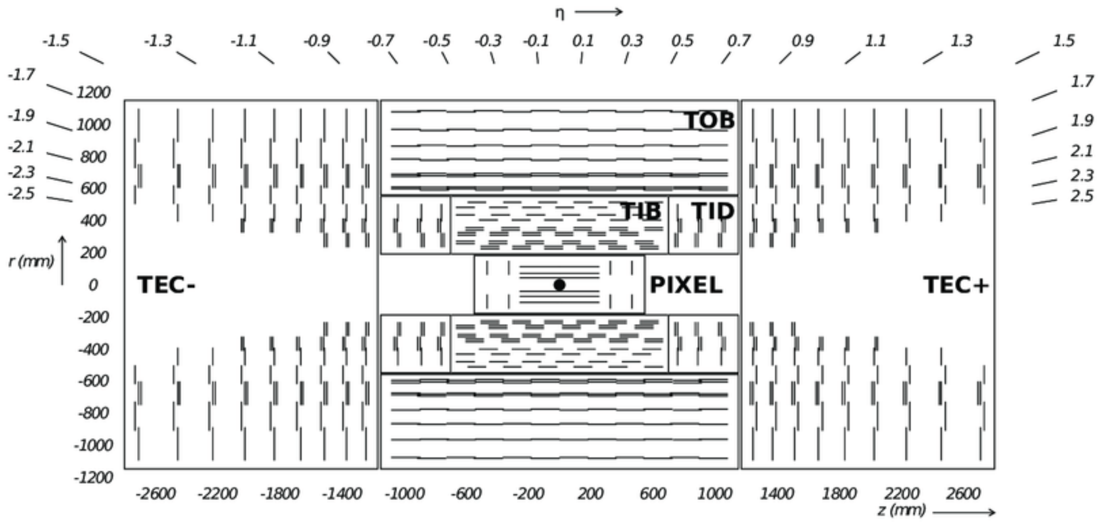

Figure 6.4: A longitudinal slice of the silicon tracker showing the coverage in η. TIB, TID, TOB, and TEC are sections of the strip tracker.

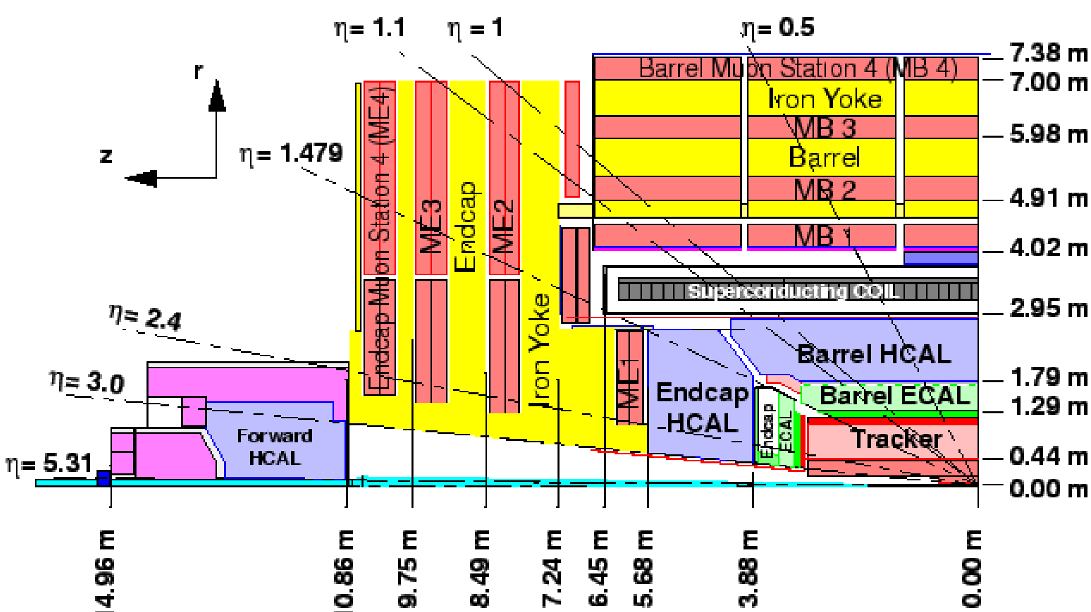

Figure 6.5: A cross sectional slice of the full detector showing the coverage in η of the muon chambers as well as other components. CMS *loves* to make acronyms for everything possible.

whose innards are constantly interacting and rearranging. In addition to the three valence quarks, these protons contain what is often called a "sea" of non-valence quarks, anti-quarks, and gluons. When two protons collide at a certain energy, we do not know a priori which fundamental particles start the interaction, or what fraction of a proton's energy those fundamental constituents contain. Instead, this can only be known probabilistically, meaning a large amount of data or *luminosity* is needed for most precise observations.

The collision of two proton bunches is referred to as a bunch crossing, and each of these results in dozens of interactions along the beam axis within the CMS detector. Due in part to the wide range of possible energies of the fundamental participants, the vast majority of interactions which occur in any bunch crossing are physically uninteresting. Some are elastic collisions which do not break apart the protons, and others are simply inelastic collisions that do not aid in making new physics measurements. In order to filter out these events from the enormous amount of data that is produced during each second of data collection, a multi-tier trigger system selects interesting events on the fly, preventing a wildly impractical amount of data from being stored permanently. For the purpose of this thesis, we will only refer explicitly to the high-level triggers, which are used to compile different datasets used for physics analysis as in Chapter 7. The potential for overlap between individual interactions taking place very close to each other creates an issue called pileup. Generally speaking, this will involve a small number of physically uninteresting events whose byproducts sneak into the data, an effect that is accounted for in simulation.

When an event is reconstructed, the negative vector sum of all transverse momenta is designated as $p_{\mathrm{T}}^{\mathrm{miss}}$ and is for historical reasons often referred to as the MET or *missing transverse energy*. This vector, in principle, corresponds to momentum that was carried off from an interaction without being detected. While there will always be some small transverse momentum imbalance due to detector effects, this quantity can be quite large if undetectable particles such as neutrinos are produced in the event.

6.4 Simulation of CMS events

Probabilities of different proton constituents interacting, and the energy they carry, are determined from *parton distribution functions*. These have been derived and tuned from many experiments over time, and multiple sets are available.

Starting from the fundamental constituents of quarks and gluons, individual collision interactions or *events* are simulated in a series of stages. First, a fixed order perturbative QFT calculation is performed to evaluate the relevant matrix element. While this process models the fundamental interaction taking place at short scales, a variety of QCD effects beyond perturbative hard scattering must be taken into account in order to make the simulation more realistic.

The first of these is emission of lower energy particles, such as gluons and photons. Because of the large value of the strong coupling constant α_s, there is a strong tendency for the high-energy participants in an interaction to radiate away some energy as a shower of lower-energy particles. Luckily, there are some mathematical methods in QCD that allow one to calculate series of such emissions to partially model this effect. The second is the non-perturbative effect of hadronization which affects quarks and gluons. These particles can travel only very short distances before they form more stable bound-state particles, like exotic hadrons and mesons, which can go on to interact with the detector. Both showering and hadronization effects are modeled by *parton shower* algorithms, which take a hard interaction involving a small number of fundamental particles and turn it into myriad of more stable objects capable of reaching the detector. The matching of shower simulations to matrix element computations is nontrivial, and multiple approaches are available.

Lastly, the detector response to all simulated events is modeled with the GEANT4 software toolkit [44], which simulates the interaction of particles with a variety of materials. While the previous steps can be run by individuals with access to reasonable computing resources, this step is very computationally expensive. For this reason, only essential samples are generated including full detector response, and we sometimes have to make due with having lower statistics in some samples than what is desirable.

Event simulation is typically done individually for specific processes and decay channels. However, the potential effects of generic physics events with overlapping primary vertices are later added into the simulation by including extra pileup events.

Chapter 7

A new measurement of the top Yukawa coupling

7.1 Electroweak corrections and $t\bar{t}$ production

Recall from Sec. 5.3 that top pair production at CMS is simulated based on matrix element calculations performed at order $\mathcal{O}(\alpha_s^3)$. This includes only effects from QCD interactions, which are by far the dominant means of production and generally much stronger than other interactions at high energy scales. Electroweak (EW) contributions begin to have a noticeable effect at order $\mathcal{O}(\alpha_s^2\alpha)$. Here we note that α stands in for the suite of EW interactions, as the weak and electromagnetic interaction couplings are related and of the same magnitude. Additionally, we will treat equally at this order diagrams with EW interactions that carry a factor of the Yukawa coupling Y_t rather than an explicit factor of α to be of this order. This allows us to consider one-loop diagrams such as those in Fig.7.1 which include Higgs

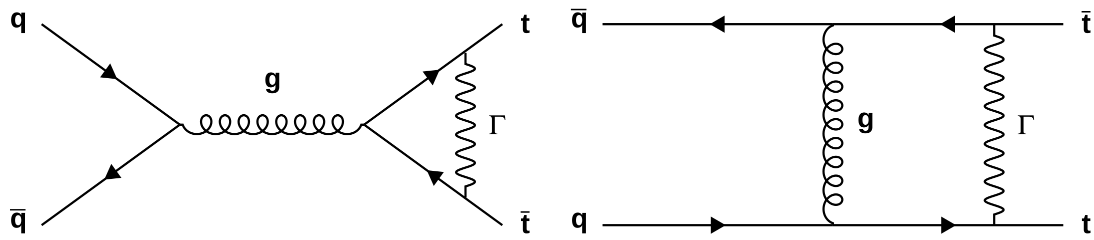

Figure 7.1: $t\bar{t}$ production from qq processes with virtual exchange of a vector or scalar boson Γ, such as the Higgs

exchange. Such diagrams are included as interference terms to obtain the leading correction, hence the lone factor of α–the one-loop term diagram interferes with the LO diagram, while its square is ignored.

We refer to the diagrams in Fig.7.1 as *EW corrections* to $t\bar{t}$ production. Their effect on the total cross section is small, so they are typically ignored. Howerver, if the Yukawa coupling entering these corrections via Higgs exchange is anomalously large, these diagrams can have a measurable effect on differential cross sections. For example, doubling the value of g_t can alter the $M_{t\bar{t}}$ distribution by about 10% near the production threshold as described in [45] and shown in Figure 7.2 (left). Another variable sensitive to the value of g_t is the difference in rapidity between top and anti top quarks $\Delta y_{t\bar{t}} = y(t) - y(\bar{t})$, shown in Figure 7.2 (right). Together, these two variables serve as proxies for the traditional Mandelstam variables s and t, and can be used to include the EW corrections on arbitrary samples via weights without generating new MC samples.

This is achieved by applying weight corrections to the current standard $t\bar{t}$ MC samples used by the CMS TOP group. Contributions to the top quark pair production due to the interference of QCD+EW diagrams, shown in Figure 7.1, with the leading order (LO) QCD diagrams are evaluated using HATHOR (v2.1) pack-

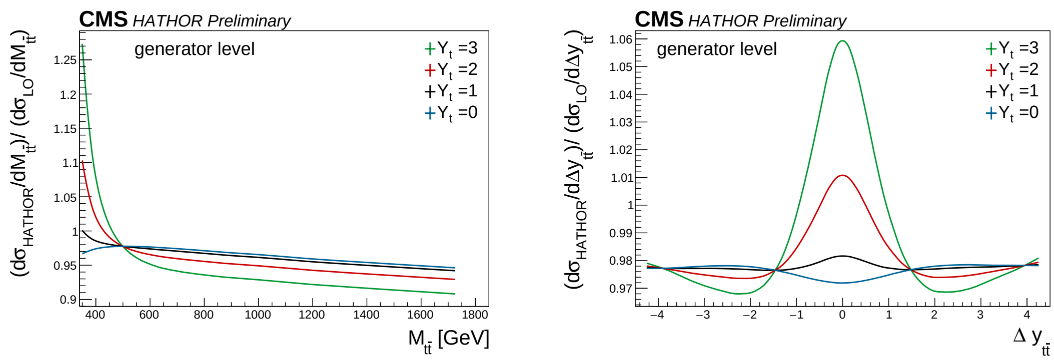

Figure 7.2: Effect of the weak corrections on $t\bar{t}$ differential cross sections for different values of Y_t, after reweighting of generator-level events from Powheg+Pythia8

age [46]. The ratio of these contributions to the LO QCD production is applied as parton-level weight corrections to events simulated using POWHEG+PYTHIA8, which incorporates fully NLO QCD calculations and parton shower effects

7.2 formalism of Weak corrections

The standard jargon of perturbation theory can sometimes be confusing, when applied to the EW corrections, since perturbative expansions are done in orders multiple separate coupling constants, principally α_s and α. We will include top-Higgs vertices as contributing an order α for notational simplicity, as they are part of the electroweak interaction. Then it is not immediately clear what is meant when someone says "NLO EW diagrams," for example. To clarify, we will utilize notation similar to [47], where a generic observable $\Sigma^{t\bar{t}}$ is expanded in a series as

$$\Sigma^{t\bar{t}}(\alpha_s, \alpha) = \sum_{m+n\geq 2} \alpha_s^m \alpha^n \Sigma_{m,n} \tag{7.1}$$

In practice, contributions due to terms with $m < 2$ or $n > 2$ are small, and as such often neglected in the calculation of the differential cross sections. In this analysis the following contributions are of interest:

$$\begin{aligned}
\Sigma_{\text{LO QCD}} &= \alpha_s^2 \Sigma_{2,0} && (7.2)\\
\Sigma_{\text{NLO QCD}} &= \alpha_s^3 \Sigma_{3,0} && (7.3)\\
\Sigma_{\text{NLO EW}} &= \alpha_s^2 \alpha \Sigma_{2,1} && (7.4)\\
\Sigma_{\text{extra EW}} &= \alpha_s^3 \alpha \Sigma_{3,1} && (7.5)
\end{aligned}$$

In using the Hathor package to compute the differential cross section, as a function of Y_{t}, we include the terms

$$\Sigma_{\text{HATHOR}}(Y_{\mathrm{t}}) = \Sigma_{\text{LO QCD}} + \Sigma_{\text{NLO EW}}(Y_{\mathrm{t}}). \tag{7.6}$$

The EW corrections K-factor can be defined at the LO QCD level:

$$K_{\text{EW}}^{\text{NLO}} = \frac{\Sigma_{\text{LO QCD}} + \Sigma_{\text{NLO EW}}}{\Sigma_{\text{LO QCD}}} \tag{7.7}$$

Meanwhile, the POWHEG +PYTHIA8 samples include terms

$$\Sigma_{\text{POWHEG}} = \left(\Sigma_{\text{LO QCD}} + \Sigma_{\text{NLO QCD}}\right)_{+\text{PS}} \tag{7.8}$$

here the subscript $+$PS indicates that parton shower simulation has been included as well. Potential variation of these parton shower effects should be covered by the standard procedure of evaluating such uncertainties.

Since $\alpha \ll \alpha_s$, it often makes some sense to work at fixed order $m \leq N$, $n \leq 1$, rather than at $m + n \leq N$ (as mentioned in [48]). Thus, the EW corrections to the NLO QCD calculations are frequently included using the K-factor, defined at the LO QCD level:

$$\Sigma_{\text{NLO QCD}\times\text{EW}} \equiv K_{\text{EW}}^{\text{NLO}} \times \left(\Sigma_{\text{LO QCD}} + \Sigma_{\text{NLO QCD}}\right) \tag{7.9}$$

We will refer to this as the “multiplicative approximation", which is similar to the “multiplicative approach" referenced in [47], aside from the missing NNLO QCD terms, which should be covered by existing modeling uncertainty due to scale variations. This is the best approximation for EW corrections available to us, and in some kinematic regimes these corrections do indeed factorize in this way from their QCD counterparts. Thus, this approach allows us to roughly approximate the terms in $\Sigma_{\text{extra EW}}$ in addition to those directly generated in HATHOR. Specific to this analysis is the dependence of Higgs-based contributions on Y_{t} and the use of POWHEG, so we can write out our formula for observables more explicitly as

$$\Sigma_{\text{NLO QCD}\times\text{EW}}^{Y_{\text{t}}} \equiv K_{\text{EW}}^{\text{NLO}}(Y_{\text{t}}) \times \Sigma_{\text{POWHEG}}. \tag{7.10}$$

In order to estimate the uncertainty on this approach to including EW corrections, we investigate also the more naive additive approach,

$$\Sigma_{\text{NLO QCD+EW}}^{Y_{\text{t}}} \equiv \left(K_{\text{EW}}^{\text{NLO}} \times \Sigma_{\text{LO QCD}}\right) + \Sigma_{\text{NLO QCD}}, \tag{7.11}$$

which neglects the term $\Sigma_{\text{extra EW}}$ entirely. We take the difference between the two approaches as an uncertainty of the method:

$$\begin{aligned} \text{EW unc.} &= \Sigma^{Y_t}_{\text{NLO QCD}\times\text{EW}} - \Sigma^{Y_t}_{\text{NLO QCD+EW}} && (7.12)\\ &= \left(\Sigma_{\text{POWHEG}} - \Sigma_{\text{LO QCD}}\right)\left(K^{\text{NLO}}_{\text{EW}}(Y_t) - 1\right) && (7.13)\\ &\equiv \Sigma_{\text{POWHEG}} \times \delta_{\text{QCD}} \times \delta_{\text{EW}}, && (7.14) \end{aligned}$$

where we have introduced the shorthand

$$\delta_{\text{QCD}} = \frac{\Sigma_{\text{POWHEG}} - \Sigma_{\text{LO QCD}}}{\Sigma_{\text{POWHEG}}}, \quad \delta_{\text{EW}} = (K^{\text{NLO}}_{\text{EW}}(Y_t) - 1), \tag{7.15}$$

to illustrate that this uncertainty is effectively a cross term which arises from the difference in additive and multiplicative approaches. Note that δ_{EW} represents the usual marginal effect in terms of which EW corrections are often understood.

The implementation of this uncertainty is detailed further in Section 7.5.

7.3 Object & event selection

Backgrounds for $t\bar{t}$ events in the dilepton channel are low due to the presence of 2 high-p_T leptons and 2 b-jets in the final state, which together are an ample signature to identify the process with high confidence. Backgrounds can thus be sufficiently modeled with simulated events, as opposed to data-driven estimation. The main backgrounds are single top production and Drell-Yan decays, examples of which are shown in Figure 7.3. Single top production simulated at NLO with POWHEG in combination with PYTHIA8, while rare diboson events are simulated in PYTHIA8 with LO precision. Drell–Yan production is simulated at LO using the MADGRAPH generator [49] interfaced to PYTHIA8 with the MLM matching algorithm [50]. Overall, after event selection, the expected non-$t\bar{t}$ background rate in this channel is about 5%.

Events are selected first using single electron or single muon triggers, designed to pick out events with at least one high-p_T lepton from the data. In the case of muons, we select events with a trigger p_T threshold of 24 GeV except in 2017 data, where the threshold is raised to 27 GeV. For electrons, we select events with a trigger p_T threshold of 27 GeV with the exception of 2018 when a threshold of 32 GeV is used due to availability. While dilepton triggers are also available with lower p_T thresholds, we found that they have no significant benefit in our case, as most events which interest us have a leading lepton p_T over 30 GeV.

To ensure that all electrons and muons are within the silicon tracker coverage, we require they have pseudo-rapidity $|\eta| < 2.4$. To operate well above the online trigger threshold, we then require at least one isolated electron or muon reconstructed with $p_T > 30$ GeV, except in 2018, where offline selection of leading electrons is

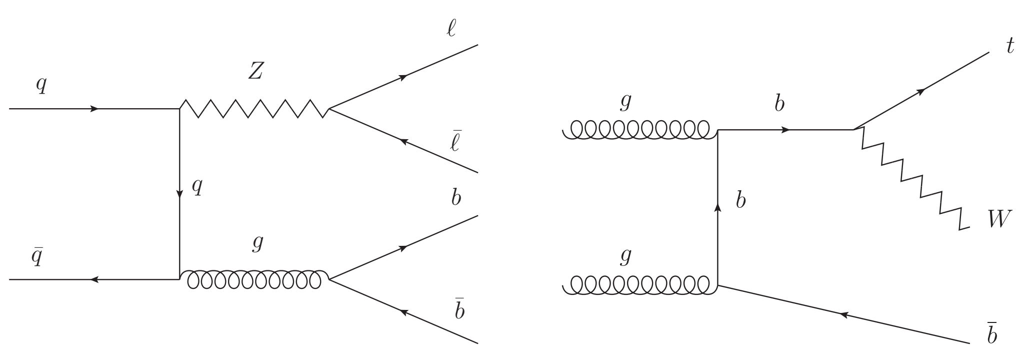

Figure 7.3: Examples of background processes for $t\bar{t}$ dilepton decays are shown. The left diagram shows a Drell-Yan process involving a Z boson decaying to a lepton + anti-lepton pair, while the right diagram shows an example of single-top production.

raised to $p_{\mathrm{T}} > 34\,\mathrm{GeV}$ to match available triggers. A small buffer of a few GeV between the online trigger selection and the offline p_{T} selection helps prevent potential disagreement between simulation and data near the trigger threshold. A second isolated electron or muon with $p_{\mathrm{T}} > 20\,\mathrm{GeV}$ is required. Any multi-lepton events with additional isolated leptons having $p_{\mathrm{T}} > 15\,\mathrm{GeV}$ are discarded.

Jets are clustered from particle-flow objects through the anti-$\mathrm{k_T}$algorithm [51,52] using a distance parameter of 0.4. The jet momentum is calculated by taking the vector sum of momenta over all constituents identified as part of the jet. Important corrections to the jet energy are derived as a function of jet p_{T} and η, using both simulation and measurements of energy balance in data [53]. We select jets with $\mid \eta \mid < 2.4$ and $p_{\mathrm{T}} > 30\,\mathrm{GeV}$. We identify jets originating from b quarks using the DeepCSV algorithm [**?**], requiring all events to have at least two b-tagged jets according to the “loose" working point, which has the highest sensitivity. Events with more than two b jets are considered only if exactly two of the jets pass a more stringent selection. In this case these two jets passing the more stringent requirement are assumed to be those originating from top quark decays.

We find that in $\mathrm{t\bar{t}}$ events, the two b jets are among the candidates passing the looser b-tagging requirement in roughly 93% of the events.

Drell-Yan background events (as in Figure 7.3 left), mostly involving the decay of a Z boson, make a substantial contribution to the ee and $\mu\mu$ channels. To reduce their prevalence, we reject events with an invariant mass of the two leptons below 50 GeV or within 10 GeV around the Z boson mass of 91.2 GeV.

The breakdown of expected signal and background yields for each year is shown in Tab. 7.1. The Drell–Yan and Single top quark production processes each account

Source	2016 (X fb^{-1})	2017 (Y fb^{-1})	2018 (Z fb^{-1})	All (X+Y+Z fb^{-1})	% total MC
$t\bar{t}$ MC	140 831±134	170 554±95	259 620±146	571 005±220	96.1%
V + jets MC	1944±54	3178±75	4958±133	10 080±162	1.7%
Single t MC	3022±25	3521±24	5827±32	12 370±47	2.1%
Diboson MC	142±9	151±10	250±15	543±20	0.1%
Total MC	145 940±148	177 404±124	270 655±201	593 999±279	100%
Data	144 817	178 088	264 791	587 696	98.9%

Table 7.1: MC and data event yields for all three years and combined. Statistical uncertainty on simulated event counts is given. For an estimate of systematic uncertainty, see Figures 7.5-7.7.

for roughly 2% of the estimated sample composition. Diboson decays, as well as other multi-jet events typically referred to as QCD background, make negligible contributions.

Additionally, there are multiple small discrepancies in efficiency when one applies the same selection criteria to simulation and data. This applies to the single lepton triggers, lepton identification, and b-jet identification. These disagreements are addressed via scale factor corrections to the event weights, which can be derived by comparing data and simulation in special cases–for example, the tag and probe method on Z decays is used for lepton-associated scale factors [54, 55]. Uncertainty on these corrective scale factors is addressed in Section 7.6

7.4 Event Reconstruction

While it is possible to completely reconstruct the neutrino momenta as described in Section 5.4, such reconstruction is highly sensitive to the MET ($p_{\mathrm{T}}^{\mathrm{miss}}$). Because the MET computation for each event relies on measurements taken throughout the detector and involving many different particles, it is vulnerable to large resolution effects and also systematic uncertainty resulting from the energy scales of various particles. For this reason, it was decided to forgo the full top quark reconstruction, instead defining proxy variables for $M_{\mathrm{t\bar{t}}}$ and $\Delta y_{\mathrm{t\bar{t}}}$. We found that a more sensitive measurement results from using the variables

$$\begin{aligned} M_{\mathrm{b}\ell} &= M(b+\bar{b}+\ell+\bar{\ell}), && (7.16) \\ |\Delta y|_{\mathrm{b}\ell} &= |y(b+\bar{\ell})-y(\bar{b}+\ell)|, && (7.17) \end{aligned}$$

which were found to have good sensitivity to EW corrections while being less vulnerable to resolution effects and systematic uncertainties. $M_{\mathrm{b}\ell}$ has the advantage of not dependening on the pairing of b jets with leptons at W decay vertices, meaning that it is reconstructed quite accurately. We do however utilize the kinematic constraints discussed in Section 5.4 to help with this pairing of b jets and leptons in order to reconstruct $\Delta y_{\mathrm{b}\ell}$. Including this variable was shown to add additional sensitivity, despite some resolution effects.

The full procedure for b-jet pairing is as follows:

1. The mass constraint is checked for both possible pairings. If only one pairing is found to satisfy the mass constraint, that pairing is used. If both pairings fail to satisfy the mass constraint, the event is discarded. If both pairings satisfy the mass constraint, we check the MET constraint.

2. If only one pairing allows for the MET constraint while the other does not, the pairing yielding an exact solution to the MET constraint is used.

3. If the neutrino kinematics do not suggest a clear pairing, the b-jets, b_1 and b_2, are paired with the leptons $(l, \bar{l})$ by minimizing the quantity

$$\Sigma_{1(2)} = \Delta R(b_{1(2)}, l) + \Delta R(b_{2(1)}, \bar{l})$$

among the two possible pairings. This method will choose the correct pairing with 74% accuracy if both b-jets have been identified correctly.

In the end, the correct b-jet pairing is selected for approximately 82% of events in which both b-jets have been correctly identified.

The sensitivity of our chosen kinematic variables to Y_{t} is shown before and after reconstruction in Figure 7.4 . The effect of Y_{t} remains substantial enough, and unique enough in shape, that a measurement can be extracted. When looking back at Figure 7.2, we see that most sensitivity in $M_{\mathrm{t\bar{t}}}$ is more narrowly confined to the threshold region, which is particularly difficult to reconstruct accurately in the dilepton channel. By comparison, the sensitivity of Y_{t} to $M_{\mathrm{b}\ell}$ is distributed across a wider region.

We also see that sensitivity to our parameter of interest Y_{t} is not greatly reduced by the reconstruction process. This stands in contrast to typical attempts to reconstruct $M_{\mathrm{t\bar{t}}}$, where the sensitivity is confined to a narrow peak at the threshold and much information is lost to resolution effects.

The comparison between data and Monte Carlo is shown in Figures 7.5-7.7. The agreement is generally seen to be well within known uncertainty. We do see some slopes in the ratio of data to MC prediction in the distributions of lepton and b-jet p_{T}, to varying extent for each year. These are likely related to a well know disagreement in top quark p_{T} distribution between POWHEG samples and data.

After reconstruction, events in each year are separated into two $|\Delta y|_{\mathrm{b}\ell}$ bins and binned more finely in the $M_{\mathrm{b}\ell}$ variable. The predominant sensitivity to Y_{t} comes from shape distortions to the $M_{\mathrm{b}\ell}$ distribution, but the additional separation by $\Delta y_{\mathrm{b}\ell}$ helps to distinguish these shape distortions from those associated with systematic

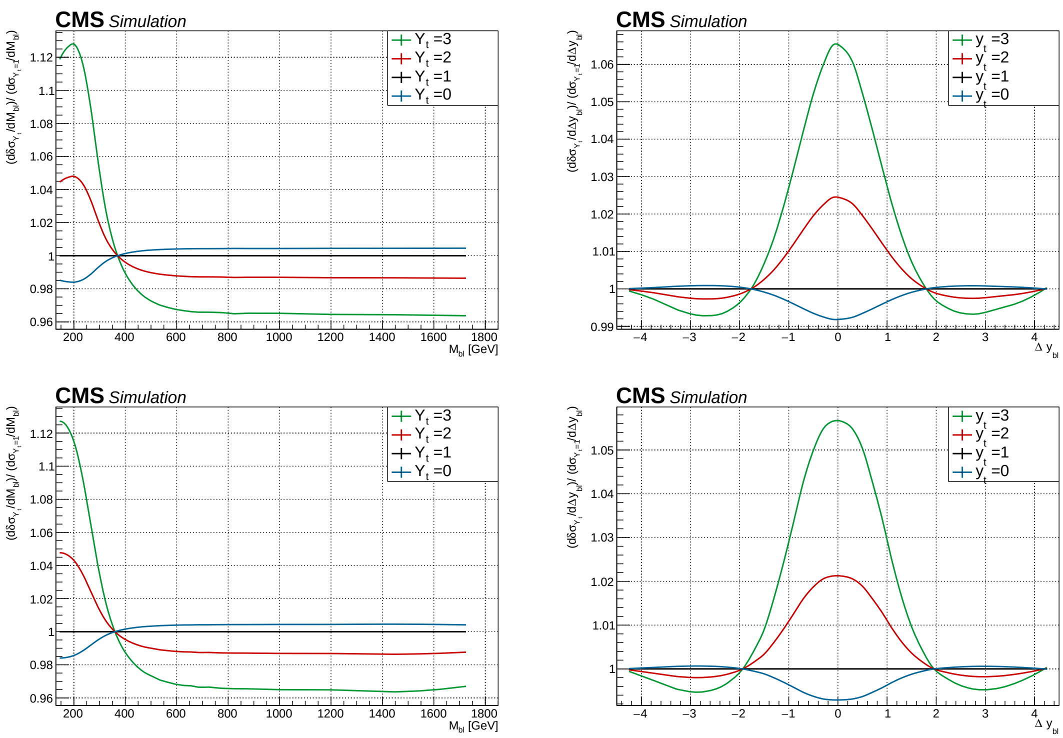

Figure 7.4: Effect of the EW corrections on $M_{\mathrm{b}\ell}$ and $\Delta y_{\mathrm{b}\ell}$ kinematic distributions are shown at generator level (top plots) and reco level (bottom plots). The effect is shown relative to the Standard Model EW corrections, as this is the best way to assess our sensitivity to different Yukawa coupling values, rather than comparing to a sample with no EW corrections.

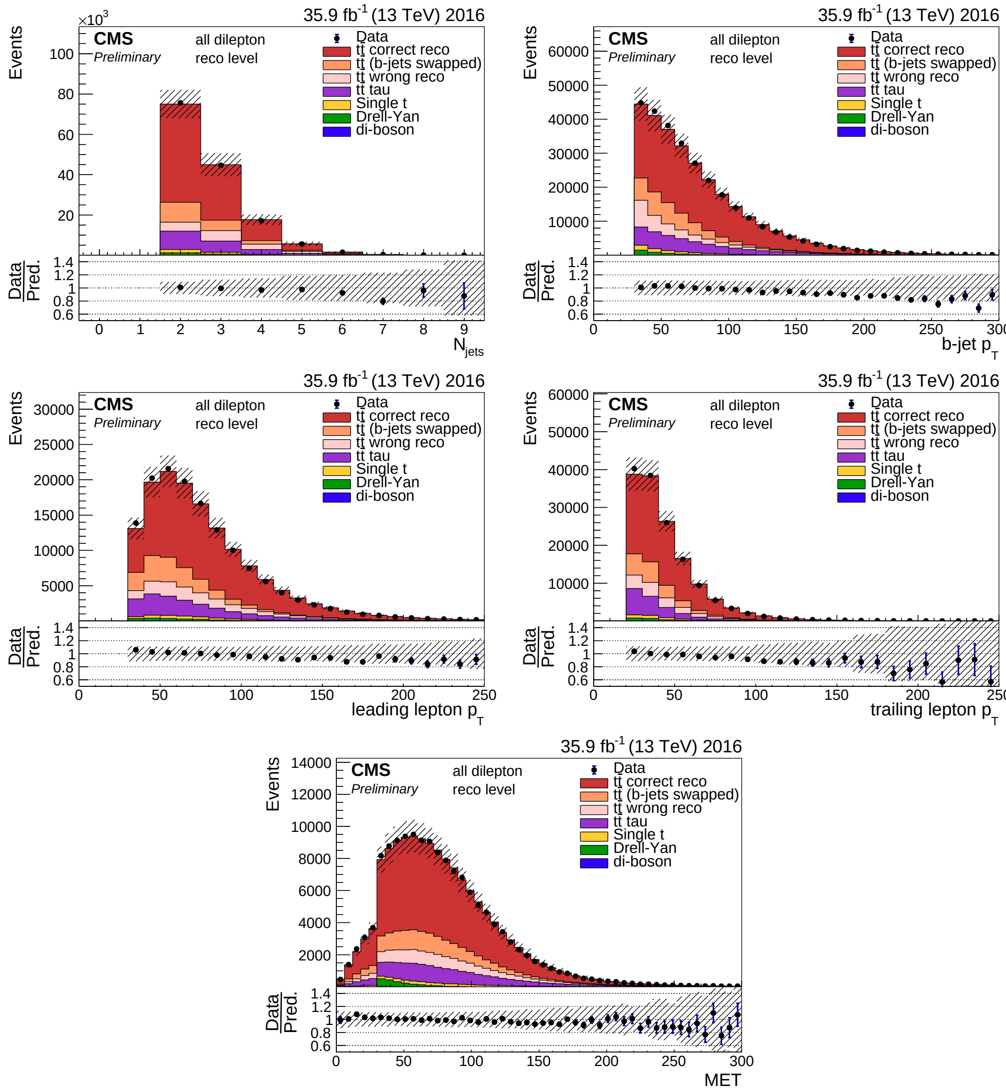

Figure 7.5: 2016 Data to MC comparison, with the shaded region indicating known uncertainty.

uncertainties. The precise binning is chosen to obtain optimal information about shape variation while maintaining low statistical uncertainty by requiring $\gtrapprox 10,000$ events present in each year in each bin. The data and simulation is shown with the final binning in Figure 7.8.

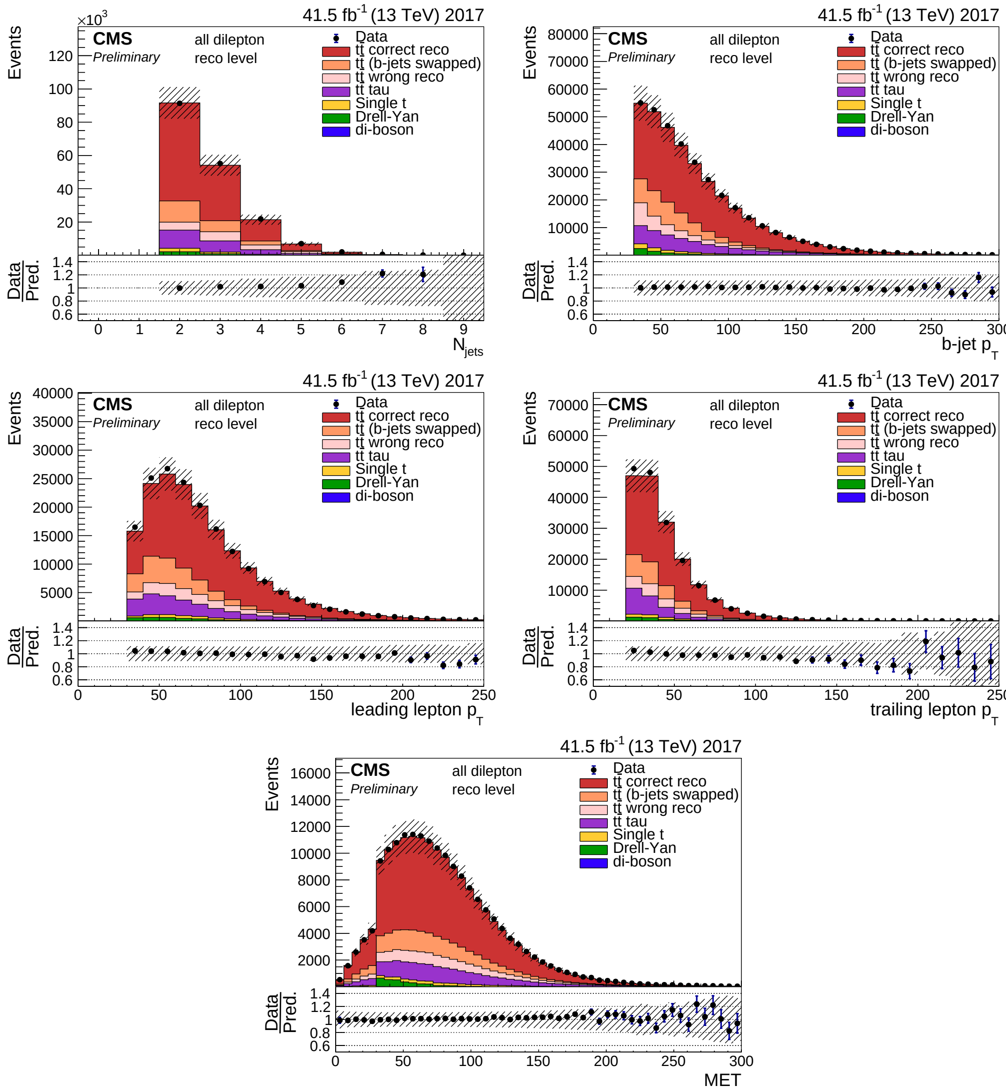

Figure 7.6: 2017 Data to MC comparison, with the shaded region indicating known uncertainty.

7.5 Statistical methods

We define a likelihood function $\mathcal{L}$, which itself is defined as a product over separate likelihood functions evaluated at each bin,

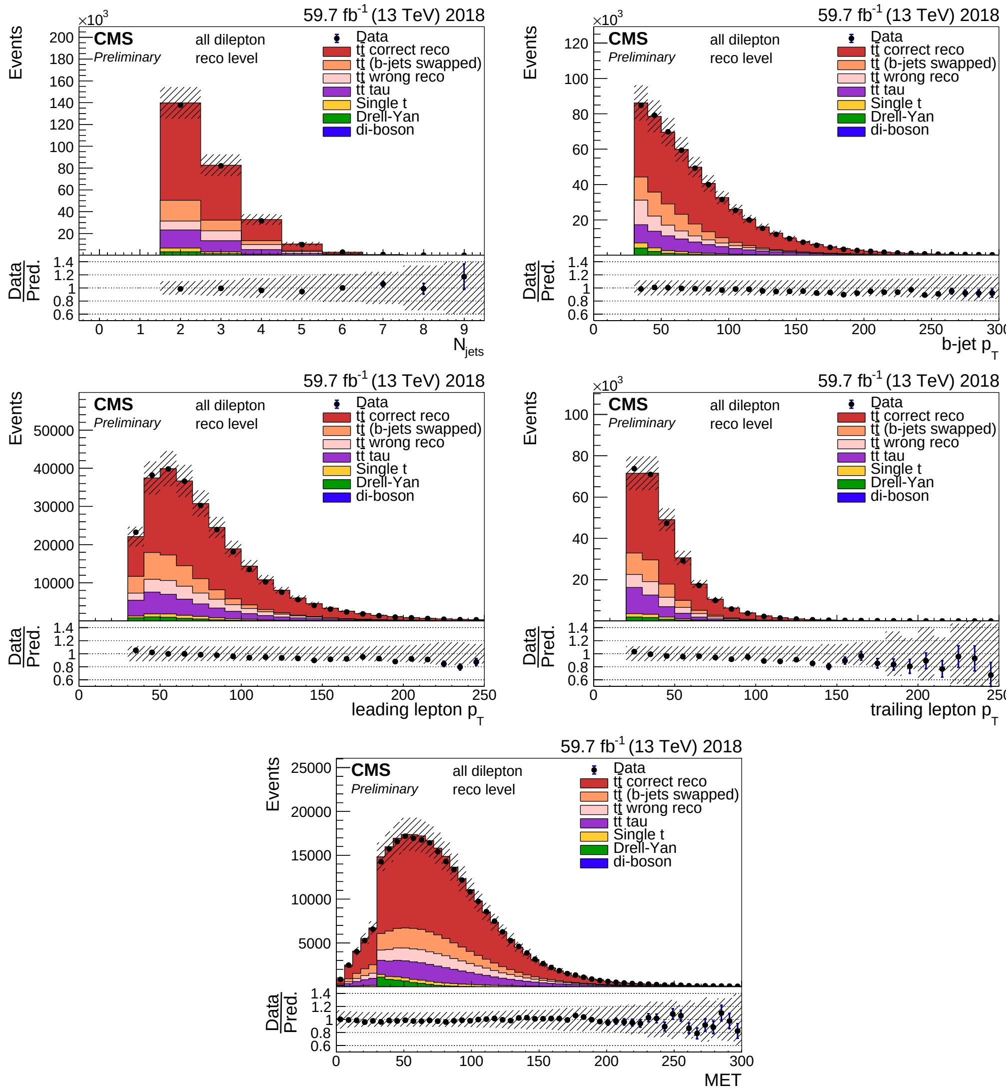

Figure 7.7: 2018 Data to MC comparison, with the shaded region indicating known uncertainty.

$$\mathcal{L} = \prod_{\text{bin} \in (M_{b\ell}, |\Delta y|_{bl})} \mathcal{L}_{\text{bin}} \,. \tag{7.18}$$

The likelihood in each bin is a product of the Poisson distribution which describes the statistical fluctuation of the event count, and a penalty term for nuisance param-

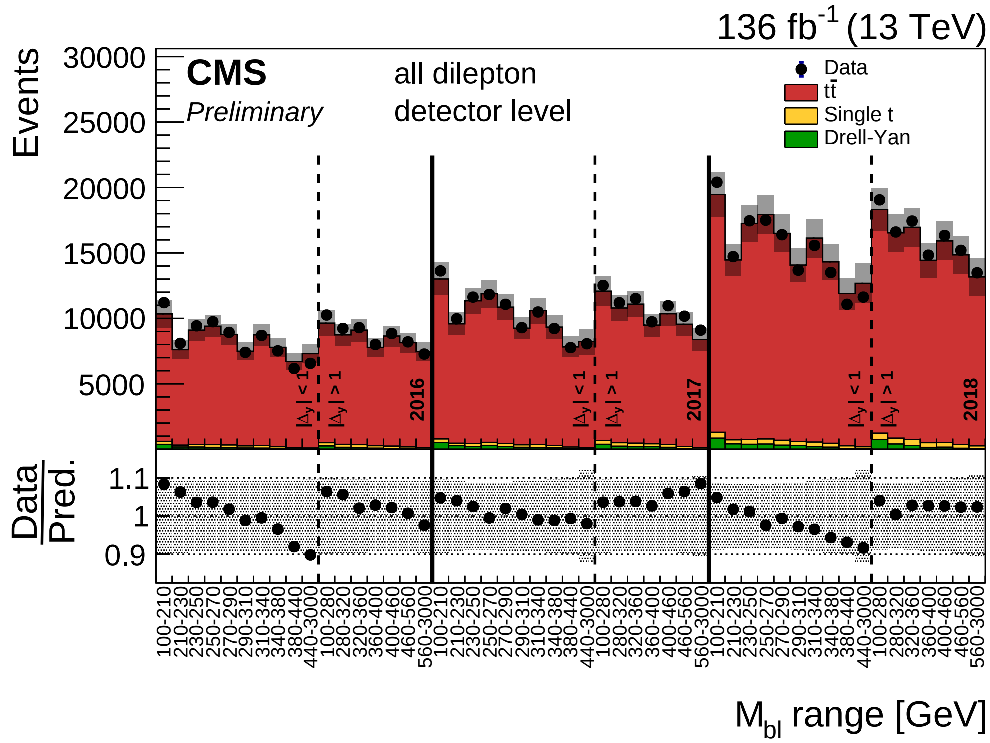

Figure 7.8: Binned data and simulated events prior to performing the statistical fit. The dashed line divides the two $|\Delta y|_{b\ell}$ bins, while the horizontal axis shows the bins' $M_{b\ell}$ ranges.

eters which represent systematic sources of uncertainty:

$$\mathcal{L}_{\text{bin}} = \text{Poisson}\left[n_{\text{obs}}^{\text{bin}}\middle|s^{\text{bin}}(\{\theta_i\}) \times R_{\text{EW}}^{\text{bin}}(Y_{\text{t}}, \phi) + b^{\text{bin}}(\{\theta_i\})\}\right] \times p(\phi) \times \prod_i p(\theta_i). \tag{7.19}$$

Here $n_{\text{obs}}^{\text{bin}}$ is the total observed bin count, with the expected bin count being the sum of the predicted signal s^{bin} and background b^{bin}. The number of expected signal events is modified by the additional rate R_{EW}, which encodes the EW corrections depends on the Yukawa coupling ratio Y_{t} and the special nuisance ϕ. The full expression for the rate $R_{\text{EW}}^{\text{bin}}$, including the modifying factor from this uncertainty, is

$$R_{\text{EW}}^{\text{bin}}(Y_{\text{t}}, \phi) = (1 + \delta_{\text{EW}}^{\text{bin}}(Y_{\text{t}})) \times (1 + \delta_{\text{QCD}}^{\text{bin}}\delta_{\text{EW}}^{\text{bin}}(Y_{\text{t}}))^{\phi}, \tag{7.20}$$

where $\delta_{\text{QCD}}^{\text{bin}}\delta_{\text{EW}}^{\text{bin}}$ represents the cross term arising from the difference in multiplicative and additive approaches of applying EW corrections as described in Section 7.1. The normally distributed nuisance parameter ϕ modulates this uncertainty.

Each of the other nuisance parameters, θ_i, represents an unknown parameter that can alter the expected bin counts. These are described by a standard normal gaussian probability distribution function of $p(\theta_i)$, often called a penalty term, that affects the likelihood when this parameter deviates from our best-estimate value.

The effects resulting from nuisance parameters $\{\theta_i\}$ are modeled by generating up and down variations of the bin content s^{bin} for each θ_i in each. These variations result from changing the underlying physical/technical sources, which are outlined in Section 7.6, usually by an amount of one standard deviation (σ) based on the uncertainty in our best estimates.

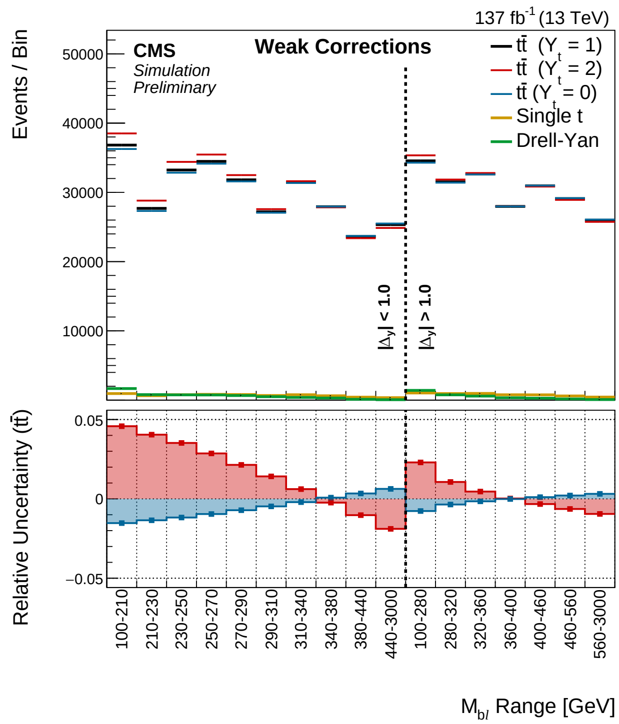

Figure 7.9: The effect of the yukawa parameter Y_t on binned reconstructed events is shown for two discrete choices of Y_t. Data from the full Run 2 period is combined in the kinematic binning.

Collectively, the up or down variation across all bins generates a shape template associated with the nuisance parameter. These shape templates are then enforced as the bin modifiers associated with $\theta_i = \pm 1$, while $\theta_i = 0$ corresponds to the nominal estimate at which simulated data is produced.

An example of a shape template for one year of data, compared to the effect of the parameter of interest (POI), are shown in Fig. 7.9. The Quadratic dependence of the electroweak corrections on individual bins are shown in Fig. **??**. Further examples of shape templates are shown in Section 7.7 We impose these shape templates through vertical template morphing as a function of the underlying nuisance θ_i, such that each bin the modifier is interpolated as a cubic spline for values of $\theta_i \in [-1, 1]$ and

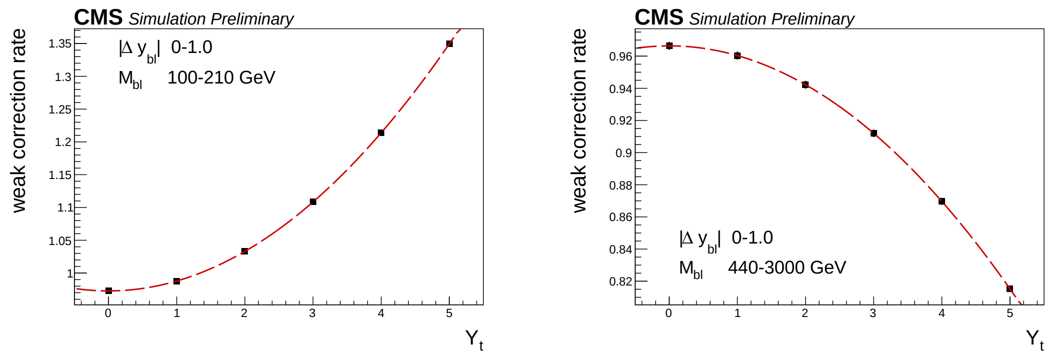

Figure 7.10: The weak correction rate modifier $R_{\mathrm{W}}^{\mathrm{bin}}$ in two separate $[M_{\mathrm{b}\ell}, \Delta y_{\mathrm{b}\ell}]$ bins from 2017 data, demonstrating the quadratic dependence on Y_{t}. All bins will have an increasing or decreasing quadratic yield function, with the steepest dependence on Y_{t} found at lower values of $M_{\mathrm{b}\ell}$.

linearly outside of that region. This is the simplest procedure available to ensure that $s^{\mathrm{bin}}(\theta_i)$ is a continuous and differentiable function.

After constructing the full likelihood function, the best-fit value of Y_{t} is obtained by maximizing the likelihood. This maximization is then repeated with Y_{t} fixed over a fine array of fixed values of the POI and comparing the maximum log likelihood, we build confidence intervals (CI) at the 68% and 95% level.

7.6 Sources of uncertainty

7.6.1 Experimental sources of uncertainty

The dominant experimental uncertainty in this analysis comes from the detector's jet energy response. Because jets are the result of clustering many individual particles, accurate measurement of the jet energy is challenging. Corrections are derived as a function of jet p_{T} and η based on simulation, which are then improved using data. We follow the standard approach outlined in [53] to consider 26 separate uncertainties which are involved in determining these calibrations. In this approach, uncertainty on the resolution of the jet reconstruction is considered as well as a separate uncertainty. When deriving shape templates for the associated uncertainties, the altered jet energy is propagated to the calculation of $p_{\mathrm{T}}^{\mathrm{miss}}$.

Other experimental sources of uncertainty are comparatively minor. The uncertainty on the integrated luminosity has an overall normalization effect on signal and background processes in each data-taking year, ranging from 2.3% to 2.5% depending on the year.

Unwanted pileup events are modeled and injected into simulation to include their effects on event reconstruction. Uncertainty on the number of pileup events included in this way is assessed by varying the inelastic cross section, 69.2 mb, by its current uncertainty of 4.6% [56].

Efficiencies in b jet identification and mis-identification are corrected, as a function of jet p_{T} and η, to better match data [28]. These uncertainties have a normalization effect of a few percent and a smaller shape component, and do not have much effect on the fit.

Similarly, scale factors are applied as functions of p_{T} and η to correct simulated efficiencies of lepton identification, isolation requirements, and triggers to match data. These are derived for muons and electrons using the tag-and-probe method on Z decays [54, 55]. The tag-and-probe fit accounts for uncertainty from statistics as well as difference in jet multiplicity. Overall, the effect is seen to be below 2%, and approximately uniform.

7.6.2 Theoretical sources of uncertainty

As a standard technique to estimate potential contributions of higher-order QCD terms at the matrix element level, the QCD renormalization scale μ_{r} and factorization scales μ_{f} are varied up and down in the POWHEG simulation by a factor of 2. The scales are each varied individually to form templates, and then a same-sign variation of the two scales together is included as an additional uncertainty. These three shape templates together cover various higher-order effects, as higher order perturbative calculations depend less and less on the scale, ultimately in principle converging to a scale-independent limit. In generating the scale variation templates, the overall normalization effect is removed, as the NNLO $\mathrm{t\bar{t}}$ cross-section is already used to improve MC normalization. This allows us to consider mainly shape effects, which we are far more sensitive to.

A 5% normalization uncertainty is included on the $\mathrm{t\bar{t}}$ cross section, which more than covers expected contribution from terms beyond NNLO QCD. The backgrounds in this analysis are small enough (each making up ≈2% or less of the expected sample composition) that we do not generate shape templates for their response to individual systematic uncertainties. We do, however, include substantial normalization uncertainties meant to broadly cover uncertainty on background modelling, which will have an effect on reconstructed distribution shapes. A 15% sample is included on single top quark production, which was seen to cover the scale variation and jet energy correction uncertainties in magnitude. A 30% normalization uncertainty is included on Drell-Yan and diboson event simulation, because these MC samples are generated with LO calculations and have larger uncertainties associated with scale variation.

We include an uncertainty on the weak corrections, based on our methods for generating and applying these additional terms, as outlined in Sections **??** and **??**. Like the scale variations, this uncertainty stands in for higher-order effects at the ME level, predominantly those coming from diagrams of order $\alpha_s^3\alpha$. This effect is included only for the region near the threshold where the EW corrections have a positive effect on the $\mathrm{t\bar{t}}$ cross section. In high-$M_{\mathrm{t\bar{t}}}$ regimes, this uncertainty would be an overestimate, as the dominant terms come from Z/W processes which factorize as Sudakov logarithms (see [47]). However, near the threshold, this is an important and fundamental uncertainty, as our sensitivity to Y_{t} comes from this region.

To model uncertainty in parton distribution functions, NNPDF set [38] provides 100 individual variations as uncertainties. As in [57], variations with similar shape templates are combined to reduce the number of variations to a more manageable 8 in total. These uncertainties are treated as fully correlated between 2017/2018 datasets, but not in the 2016 data as the simulation uses a different version of NNPDF with incompatible variations. Variation of the strong coupling constant α_s used by NNPDF is included as well. Though the these uncertainties can have significant shape effects, they are generally small, on the order of $\sim$1% or less.

Dedicated MC samples are generated with the top mass varied up and down by 1 GeV to model uncertainty on the measured top mass (though at present this value is an overestimate of that uncertainty). Due to statistical fluctuations in the dedicated samples, simulations from all three years are combined to generate one shape template, and the uncertainty is taken as correlated between years. It should be noted that, although the top mass and Yukawa coupling are generally treated independently in this measurement strategy, varying the mass will slightly modify the definition of $Y_{\mathrm{t}} = 1$. However, the effect is below 1%, making it much smaller than the sensitivity of the measurement and safe to ignore.

The h_{damp} parameter, which controls the matrix element parton shower matching in POWHEG + PYTHIA8, is varied in order to estimate the uncertainty in the matching algorithm. Dedicated MC samples are also generated with variations of the PYTHIA8 tune in order to estimate uncertainty in the hadronization model.

Uncertainty due to initial and final state radiation in the parton shower algorithms is assessed by varying the energy scale in the initial and final states by a factor of 2.

Lastly, there are two more modelling uncertainties related to b-jet modeling. The branching ratio of semi-leptonic B decays affects the b-jet response, so this quantity is varied within its measured uncertainty [58] to model its effects. Additionally, The momentum transfer from b quarks to B hadrons is dependent on the fragmentatiom rate $x_b = \frac{p_{\mathrm{T}}(B)}{p_{\mathrm{T}}(b-jet)}$. To include the uncertainty of this ratio, the transfer function is varied up and down within uncertainty of the Bowler-Lund parameter [59] in PYTHIA8 and the resulting effect is applied via event weights.

7.6.3 Processing of shape templates

Shape templates are generated for all uncertainties which are not explicitly normalization-based uncertainties. These templates are generate separately for each year, due to minor differences between data taking periods. In many cases the underlying nuisance parameter is fully or partially correlated between years, which is enforced in the likelihood fit. Some shape templates are also smoothed to eliminate noise, or made to be exactly symmetric, both of which help to ensure stability and performance of the fit. Templates which do not exhibit an effect of $> 0.1\%$ after smoothing are converted to an overall normalization uncertainty, as shape distortions are not meaningful at this level. Example shape templates are shown for the 3 dominant uncertainties in Fig. 7.11, where the effects of smoothing and symmetrizing can be seen.

7.7 Results

The maximum likelihood fit yields a best fit value of $Y_t = 1.16^{+0.24}_{-0.36}$, and a 95% CI of $Y_t \in [0, 1.62]$. Agreement of data and simulation in the final analysis binning is shown for the final configuration after performing the maximum likelihood fit in Fig.7.12. We see that the fit is able to obtain good agreement and remove sloping seen in the pre-fit data (Figure 7.8). A likelihood scan visualizing the construction of the confidence intervals is shown in Fig.7.13, performed for both data and simulation. The result is in agreement with the analogous measurement obtained previously in [57]. While it does not mark a major improvement in sensitivity, this measurement serves as a valuable complement, particularly due to the use of a different decay channel with different backgrounds.

7.8 Measurement Summary

Though we achieve lower sensitivity compared to production-based constraints in ttH [60] and Higgs combination measurements [61], it should be noted that these measurements depend as well on other Yukawa coupling values through additional branching assumptions. Thus, our result serves as a compelling orthogonal

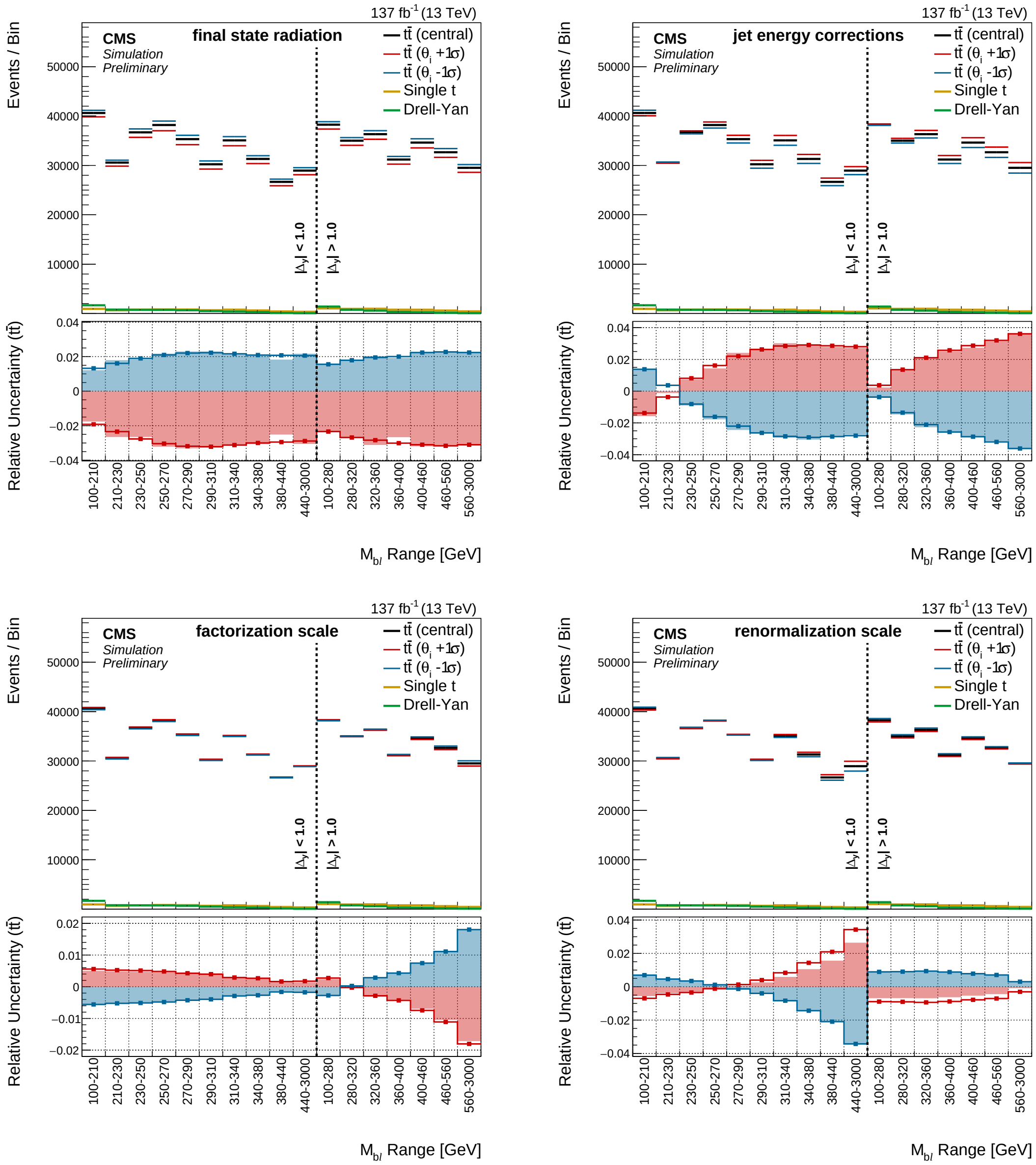

Figure 7.11: Shape templates are shown for dominant uncertainties in the fit, associated with the final-state radiation in PYTHIA8, the jet energy corrections, the factorization scale, and the renormalization scale. The shaded bars represent the raw shape template information, while the lines show the shapes after smoothing and symmetrization have been applied. In the fit, the jet energy corrections are split into 26 different components, but for brevity only the total uncertainty is shown here. Variation between years in minimal for each of these uncertainties, so their effect is shown on the full dataset in the kinematic binning, although though they are treated separately by year in the fit to ensure accurate modelling.

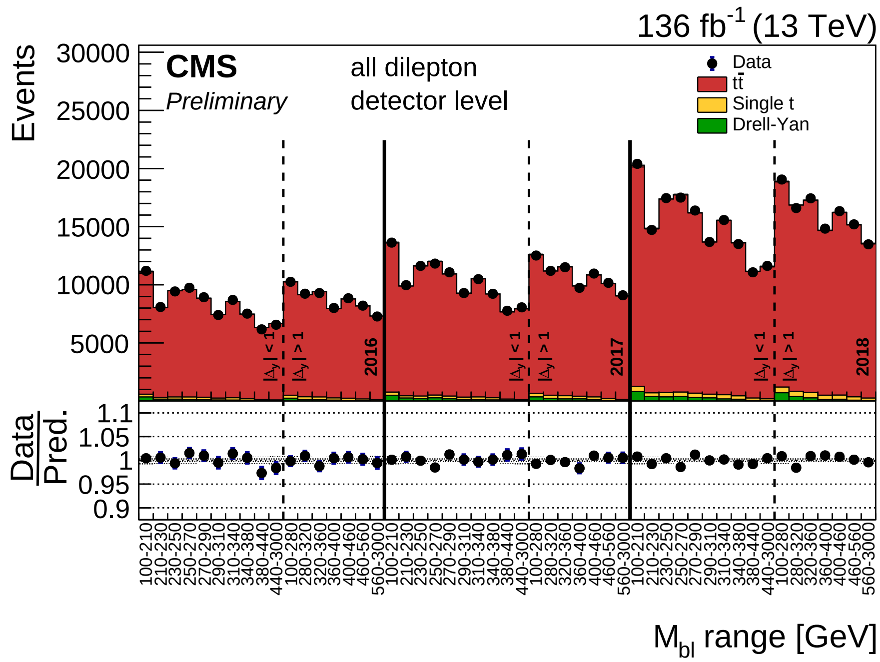

Figure 7.12: The agreement between data and MC simulation at the best fit value of $Y_t = 1.16$ after performing the likelihood maximization.

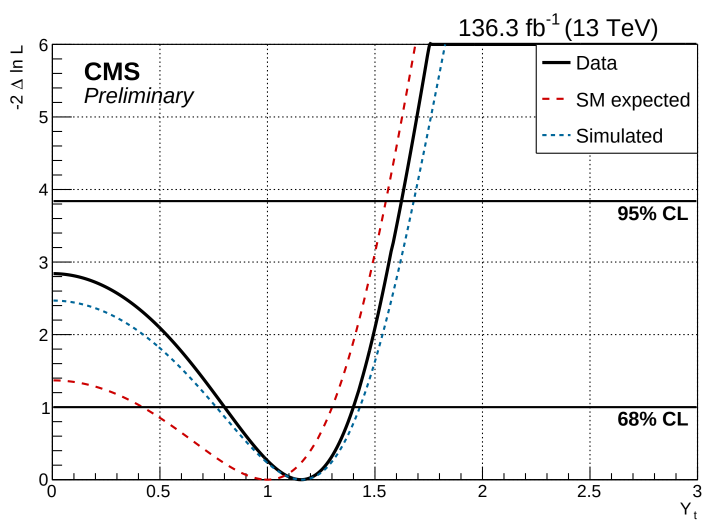

Figure 7.13: The result of a likelihood scan, performed by fixing the value of Y_t at values over the interval [0, 3.0] and minimizing the negative log likelihood ($-\ln \mathcal{L}$). Expected curves from fits on simulated data are shown produced at the SM value $Y_t = 1.0$ (red, dashed) and at the final best-fit value of $Y_t = 1.16$ (blue, dashed).

measurement to these techniques. Another recent measurement which possesses a similar independence to other branching ratios comes from searches for the production of four top quarks [62], which yields a 95% CI upper limit of $Y_t < 1.7$ [62], compared to the 95% upper limit of $Y_t < 1.62$ seen here.

Bibliography

[1] M. Czakon, D. Heymes, and A. Mitov, "High-Precision Differential Predictions for Top-Quark Pairs at the LHC", *Physical Review Letters* **116** (Feb, 2016) `doi:10.1103/physrevlett.116.082003`.

[2] A. Einstein, "Über einem die Erzeugung und Verwandlung des Lichtes betreffenden heuristischen Gesichtspunkt", *Annalen der physik* **4** (1905).

[3] C. Jönsson, "Elektroneninterferenzen an mehreren künstlich hergestellten Feinspalten", *Zeitschrift für Physik* **161** (1961), no. 4, 454–474.

[4] P. G. Merli, G. Missiroli, and G. Pozzi, "On the statistical aspect of electron interference phenomena", *Am. J. Phys* **44** (1976), no. 3, 306–307.

[5] D. Hanneke, S. F. Hoogerheide, and G. Gabrielse, "Cavity control of a single-electron quantum cyclotron: Measuring the electron magnetic moment", *Physical Review A* **83** (2011), no. 5, 052122.

[6] T. Aoyama, M. Hayakawa, T. Kinoshita et al., "Tenth-order electron anomalous magnetic moment: Contribution of diagrams without closed lepton loops", *Physical Review D* **91** (2015), no. 3, 033006.

[7] H. Georgi, "Lie algebras in particle physics: from isospin to unified theories", volume 54. Westview press, 1999.

[8] A. Zee, "Group theory in a nutshell for physicists", volume 17. Princeton University Press, 2016.

[9] H. Yukawa, "On the interaction of elementary particles. I", *Proceedings of the Physico-Mathematical Society of Japan. 3rd Series* **17** (1935) 48–57.

[10] CMS Collaboration, "Observation of a New Boson at a Mass of 125 GeV with

the CMS Experiment at the LHC", *Phys. Lett. B* **716** (2012) 30, doi:10.1016/j.physletb.2012.08.021, arXiv:1207.7235.

[11] ATLAS Collaboration, "Observation of a new particle in the search for the Standard Model Higgs boson with the ATLAS detector at the LHC", *Phys. Lett. B* **716** (2012) 1, doi:10.1016/j.physletb.2012.08.020, arXiv:1207.7214.

[12] Y. Sofue and V. Rubin, "Rotation curves of spiral galaxies", *Annual Review of Astronomy and Astrophysics* **39** (2001), no. 1, 137–174.

[13] Supernova Cosmology Project Collaboration, "Measurements of Ω and Λ from 42 high-redshift supernovae", *The Astrophysical Journal* **517** (1999), no. 2, 565.

[14] High-Z SN Search Team Collaboration, "Observational evidence from supernovae for an accelerating universe and a cosmological constant", *The Astronomical Journal* **116** (1998), no. 3, 1009.

[15] K. G. Wilson, "The renormalization group and critical phenomena", *Reviews of Modern Physics* **55** (1983), no. 3, 583.

[16] A. Kar, "Renormalization from classical to quantum physics", *University of Rochester PhD Thesis* (2014).

[17] M. Hairer, "Regularity structures and the dynamical Φ^4_3 model", *arXiv preprint arXiv:1508.05261* (2015).

[18] S. Aoki, Y. Aoki, D. Bečirević et al., "Review of lattice results concerning low-energy particle physics", *The European Physical Journal C* **77** (2017), no. 2, 112.

[19] "Millenium Problems". https://www.claymath.org/millennium-problems.

[20] R. D. Peccei, "The strong CP problem and axions", in *Axions*, pp. 3–17. Springer, 2008.

[21] M. Dine and A. Kusenko, "Origin of the matter-antimatter asymmetry", *Reviews of Modern Physics* **76** (2003), no. 1, 1.

[22] A. R. Liddle, "An introduction to cosmological inflation", *High energy physics*

and cosmology (1998) 260.

[23] A. Blondel, "Precision electroweak physics at LEP", `doi:10.1016/0920-5632(94)90655-6`.

[24] "Constraint on the matter–antimatter symmetry-violating phase in neutrino oscillations", *Nature* **580** (Apr, 2020) 339âĂŞ344, `doi:10.1038/s41586-020-2177-0`.

[25] D0 Collaboration Collaboration, "Observation of the Top Quark", *Phys. Rev. Lett.* **74** (Apr, 1995) 2632–2637, `doi:10.1103/PhysRevLett.74.2632`.

[26] CDF Collaboration Collaboration, "Observation of Top Quark Production in $\overline{p}p$ Collisions with the Collider Detector at Fermilab", *Phys. Rev. Lett.* **74** (Apr, 1995) 2626–2631, `doi:10.1103/PhysRevLett.74.2626`.

[27] M. Czakon and A. Mitov, "Top++: A program for the calculation of the top-pair cross-section at hadron colliders", *Comput. Phys. Commun.* **185** (2014) 2930, `doi:10.1016/j.cpc.2014.06.021`, `arXiv:1112.5675`.

[28] CMS Collaboration, "Identification of heavy-flavour jets with the CMS detector in pp collisions at 13 TeV", *JINST* **13** (2018) P05011, `doi:10.1088/1748-0221/13/05/P05011`, `arXiv:1712.07158`.

[29] P. Nason, "A new method for combining NLO QCD with shower Monte Carlo algorithms", *JHEP* **11** (2004) 040, `doi:10.1088/1126-6708/2004/11/040`, `arXiv:hep-ph/0409146`.

[30] S. Frixione, P. Nason, and C. Oleari, "Matching NLO QCD computations with parton shower simulations: the POWHEG method", *JHEP* **11** (2007) 070, `doi:10.1088/1126-6708/2007/11/070`, `arXiv:0709.2092`.

[31] S. Alioli, P. Nason, C. Oleari et al., "A general framework for implementing NLO calculations in shower Monte Carlo programs: the POWHEG BOX", *JHEP* **06** (2010) 043, `doi:10.1007/JHEP06(2010)043`, `arXiv:1002.2581`.

[32] J. M. Campbell, R. K. Ellis, P. Nason et al., "Top-pair production and decay at NLO matched with parton showers", *JHEP* **04** (2015) 114, `doi:10.1007/JHEP04(2015)114`, `arXiv:1412.1828`.

[33] T. Sjöstrand, S. Mrenna, and P. Skands, "PYTHIA 6.4 physics and manual", *JHEP* **05** (2006) 026, doi:10.1088/1126-6708/2006/05/026, arXiv:hep-ph/0603175.

[34] T. Sjöstrand, S. Mrenna, and P. Z. Skands, "A brief introduction to PYTHIA 8.1", *Comput. Phys. Commun.* **178** (2008) 852, doi:10.1016/j.cpc.2008.01.036, arXiv:0710.3820.

[35] R. Frederix and S. Frixione, "Merging meets matching in MC@NLO", *JHEP* **12** (2012) 061, doi:10.1007/JHEP12(2012)061, arXiv:1209.6215.

[36] P. Skands, S. Carrazza, and J. Rojo, "Tuning PYTHIA 8.1: the Monash 2013 tune", *Eur. Phys. J. C* **74** (2014) 3024, doi:10.1140/epjc/s10052-014-3024-y, arXiv:1404.5630.

[37] CMS Collaboration, "Extraction and validation of a new set of CMS PYTHIA8 tunes from underlying-event measurements", *Eur. Phys. J. C* **80** (2020) 4, doi:10.1140/epjc/s10052-019-7499-4, arXiv:1903.12179.

[38] NNPDF Collaboration, "Parton distributions for the LHC Run II", *JHEP* **04** (2015) 040, doi:10.1007/JHEP04(2015)040, arXiv:1410.8849.

[39] NNPDF Collaboration, "Parton distributions from high-precision collider data", *Eur. Phys. J. C* **77** (2017) 663, doi:10.1140/epjc/s10052-017-5199-5, arXiv:1706.00428.

[40] L. Evans and P. Bryant, "LHC Machine", *Journal of Instrumentation* **3** (aug, 2008) S08001–S08001, doi:10.1088/1748-0221/3/08/s08001.

[41] G. Roland, K. Šafařík, and P. Steinberg, "Heavy-ion collisions at the LHC", *Progress in Particle and Nuclear Physics* **77** (2014) 70–127.

[42] CMS Collaboration, "Particle-flow reconstruction and global event description with the CMS detector", *JINST* **12** (2017) P10003, doi:10.1088/1748-0221/12/10/P10003, arXiv:1706.04965.

[43] CMS Collaboration, "The CMS experiment at the CERN LHC", *JINST* **3** (2008) S08004, doi:10.1088/1748-0221/3/08/S08004.

[44] GEANT4 Collaboration, "GEANT4—a simulation toolkit", *Nucl. Instrum.*

Meth. A **506** (2003) 250, doi:10.1016/S0168-9002(03)01368-8.

[45] J. H. Kühn, A. Scharf, and P. Uwer, "Weak interactions in top-quark pair production at hadron colliders: an update", *Phys. Rev. D* **91** (2015) 014020, doi:10.1103/PhysRevD.91.014020, arXiv:1305.5773.

[46] M. Aliev, H. Lacker, U. Langenfeld et al., "HATHOR: HAdronic Top and Heavy quarks crOss section calculatoR", *Comput. Phys. Commun.* **182** (2011) 1034, doi:10.1016/j.cpc.2010.12.040, arXiv:1007.1327.

[47] M. Czakon, D. Heymes, A. Mitov et al., "Top-pair production at the LHC through NNLO QCD and NLO EW", *JHEP* **10** (2017) 186, doi:10.1007/JHEP10(2017)186, arXiv:1705.04105.

[48] D. Pagani, I. Tsinikos, and M. Zaro, "The impact of the photon PDF and electroweak corrections on $t\bar{t}$ distributions", *Eur. Phys. J. C* **76** (2016) 479, doi:10.1140/epjc/s10052-016-4318-z, arXiv:1606.01915.

[49] J. Alwall, R. Frederix, S. Frixione et al., "The automated computation of tree-level and next-to-leading order differential cross sections, and their matching to parton shower simulations", *JHEP* **07** (2014) 079, doi:10.1007/JHEP07(2014)079, arXiv:1405.0301.

[50] J. Alwall, S. Höche, F. Krauss et al., "Comparative study of various algorithms for the merging of parton showers and matrix elements in hadronic collisions", *Eur. Phys. J. C* **53** (2008) 473, doi:10.1140/epjc/s10052-007-0490-5, arXiv:0706.2569.

[51] M. Cacciari, G. P. Salam, and G. Soyez, "The anti-k_{t} jet clustering algorithm", *JHEP* **04** (2008) 063, doi:10.1088/1126-6708/2008/04/063, arXiv:0802.1189.

[52] M. Cacciari, G. P. Salam, and G. Soyez, "FastJet user manual", *Eur. Phys. J. C* **72** (2012) 1896, doi:10.1140/epjc/s10052-012-1896-2, arXiv:1111.6097.

[53] CMS Collaboration, "Jet energy scale and resolution in the CMS experiment in pp collisions at 8 TeV", *JINST* **12** (2017) P02014, doi:10.1088/1748-0221/12/02/P02014, arXiv:1607.03663.

[54] CMS Collaboration, “Performance of the CMS muon detector and muon reconstruction with proton-proton collisions at $\sqrt{s} = 13$ TeV”, *JINST* **13** (2018) P06015, doi:10.1088/1748-0221/13/06/P06015, arXiv:1804.04528.

[55] CMS Collaboration, “Performance of electron reconstruction and selection with the CMS detector in proton-proton collisions at $\sqrt{s} = 8$ TeV”, *JINST* **10** (2015) P06005, doi:10.1088/1748-0221/10/06/P06005, arXiv:1502.02701.

[56] ATLAS Collaboration, “Measurement of the inelastic proton-proton cross section at $\sqrt{s} = 13$ TeV with the ATLAS detector at the LHC”, *Phys. Rev. Lett.* **117** (2016) 182002, doi:10.1103/PhysRevLett.117.182002, arXiv:1606.02625.

[57] CMS Collaboration, “Measurement of the top quark Yukawa coupling from $t\bar{t}$ kinematic distributions in the lepton+jets final state in proton-proton collisions at $\sqrt{s} = 13$ TeV”, *Phys. Rev. D* **100** (2019) 072007, doi:10.1103/PhysRevD.100.072007, arXiv:1907.01590.

[58] Particle Data Group Collaboration, “Review of Particle Physics”, *Phys. Rev. D* **98** (2018) 030001, doi:10.1103/PhysRevD.98.030001.

[59] M. G. Bowler, “e^+e^- Production of heavy quarks in the string model”, *Z. Phys. C* **11** (1981) 169, doi:10.1007/BF01574001.

[60] CMS Collaboration, “Observation of $t\bar{t}H$ production”, *Phys. Rev. Lett.* **120** (2018) 231801, doi:10.1103/PhysRevLett.120.231801, arXiv:1804.02610.

[61] CMS Collaboration, “Combined measurements of Higgs boson couplings in proton-proton collisions at $\sqrt{s} = 13$ TeV”, *Eur. Phys. J. C* **79** (2019) 421, doi:10.1140/epjc/s10052-019-6909-y, arXiv:1809.10733.

[62] CMS Collaboration, “Search for standard model production of four top quarks with same-sign and multilepton final states in proton-proton collisions at $\sqrt{s} = 13$ TeV”, *Eur. Phys. J. C* **78** (2018) 140, doi:10.1140/epjc/s10052-018-5607-5, arXiv:1710.10614.